



An estuarine-tuned quasi-analytical algorithm (QAA-V): assessment and application to satellite estimates of SPM in Galveston Bay following Hurricane Harvey

Ishan D. Joshi and Eurico J. D'Sa

Department of Oceanography and Coastal Sciences, Louisiana State University, Baton Rouge, LA 70803, USA

Correspondence: Eurico J. D'Sa (ejdsa@lsu.edu)

Received: 5 April 2018 – Discussion started: 10 April 2018

Revised: 26 June 2018 – Accepted: 26 June 2018 – Published: 4 July 2018

Abstract. The standard quasi-analytical algorithm (Lee et al., 2002) was tuned as QAA-V using a suite of synthetic data and in situ measurements to improve its performance in optically complex and shallow estuarine waters. Two modifications were applied to the standard QAA: (1) the semi-analytical relationship for obtaining remote sensing reflectance just below the water surface as a function of absorption and backscattering coefficients was updated using Hydrolight[®] simulations, and (2) an empirical model of the total non-water absorption coefficient was proposed using a ratio of green to red bands of an ocean color sensor, which is known to work well in various inland and estuarine environments. The QAA-V-derived total absorption and backscattering coefficients, which were evaluated in a variety of waters ranging from highly absorbing and turbid to relatively clear shelf waters, showed satisfactory performance on a Hydrolight-simulated synthetic dataset ($R^2 > 0.87$, MRE $< 17\%$), an in situ estuarine and nearshore dataset ($R^2 > 0.70$, MRE $< 35\%$), and the NOMAD ($R^2 > 0.90$, MRE $< 30\%$). When compared to the standard QAA (QAA-v6), the QAA-V showed an obvious improvement with ~ 30 – 40% reduction in absolute mean relative error for the Hydrolight-simulated synthetic and in situ estuarine and nearshore datasets, respectively. The methodology of tuning QAA was applied to the VIIRS ocean color sensor and validation results suggest that the proposed methodology can also be applied to other ocean color and land-observing sensors. The QAA-V was also assessed on VIIRS imagery using a regional relationship between suspended particulate matter (SPM) and particulate backscattering coefficient at 532 nm ($b_{\text{btw}532}$; $R^2 = 0.89$, $N = 33$). As a case study, the QAA-V processing chain and VIIRS im-

agery were used to generate a sequence of SPM maps of Galveston Bay, Texas following the unprecedented flooding of Houston and the surrounding regions due to Hurricane Harvey in August 2017. The record discharge of floodwaters through two major rivers into the bay resulted in very high SPM concentrations over several days throughout the bay, with wind forcing additionally influencing its distribution into the coastal waters of the northern Gulf of Mexico. The promising results of this study suggest that the application of QAA-V to various ocean color and land-observing satellite imagery could be used to assess the bio-optical state and water quality dynamics in a variety of coastal systems around the world.

1 Introduction

Urbanization and the associated anthropogenic stressors are of major concern for the ecosystem health and water quality of estuarine environments, cumulatively affecting the coastal and marine ecosystems through estuarine–shelf exchange processes (Haynes et al., 2007; Bricker et al., 2008; Jutterström et al., 2014). Inherent optical properties (IOPs) such as absorption and backscattering coefficients have immense potential to capture changes in the bio-optical state of an aquatic system and hence provide crucial information about regional alterations in water quality associated with terrestrial pollution (Zielinski et al., 2009), harmful algal blooms (Hu et al., 2008), floods (Álvarez-Romero et al., 2013), hurricanes (Lohrenz et al., 2008; Chen et al., 2009), seasonal cycles (D'Sa and Miller, 2003; D'Sa et al., 2006; Singh et al., 2010; Joshi and D'Sa, 2015), and even human-induced

catastrophes such as oil spills (Ramsey III et al., 2011; D'Sa et al., 2016). In addition to water itself, there are three major water constituents that contribute to water-leaving radiance (L_w), namely colored dissolved organic matter (CDOM; also called “gelbstoff” or “gilvin”), suspended sediments (detritus and minerals), and phytoplankton (Naik et al., 2011). CDOM and suspended sediments are strongly associated with light absorption in the blue, and therefore high concentrations may reduce light quality for photosynthetic organisms (e.g., phytoplankton and submerged vegetation) in estuarine waters (Keith et al., 2002; Ralph et al., 2007; Pedersen et al., 2012). The effects of water turbidity caused by dissolved and particulate components on physical and behavioral changes in aquatic species have been well reported in the literature (Wang et al., 2008; Kjelland et al., 2015). Collectively, these water constituents attenuate incoming light, while a fraction of it is backscattered out of water by the water itself and particles. Therefore, deciphering L_w (or remote sensing reflectance; R_{rs}) to separate the individual contributions of optically active components may provide crucial information about the bio-optical state of a water body.

Field-based sampling methods are traditional and accurate ways to measure bio-optical properties; however, they lack adequate spatial and temporal coverage for capturing short-period bio-optical alterations and estuarine-scale dynamics. In contrast, remote sensing platforms (e.g., satellite sensors) sense L_w (or R_{rs}) signal and are advantageous over field observations in providing better synoptic spatiotemporal coverage if the signal is successfully linked to in-water IOPs. As such, satellite-based remote sensing has been widely used to monitor harmful algal blooms (Carvalho et al., 2011; Hu et al., 2016), pollution events (Mishra et al., 2013; Zhao et al., 2014), suspended sediment dynamics (D'Sa et al., 2007), CDOM distribution and carbon flux (Joshi and D'Sa, 2015; Joshi et al., 2017a), and phytoplankton biomass and primary production (Uitz et al., 2010; Matsumoto et al., 2014), as well as to evaluate the effects of climate change on exotic marine biota (Liu et al., 2006; Castillo and Lima, 2010; Cavanaugh et al., 2011; Pu and Bell, 2017).

In recent years, both empirical and semi-analytical models have been frequently used to link satellite observations and in-water properties, such as IOPs, vertical diffuse attenuation coefficients (K_d), suspended particulate matter (SPM) concentrations, CDOM, pigment concentrations, phytoplankton cell counts and cell size, and particle size (D'Sa et al., 2003, 2006, 2007; Pan et al., 2010; Chen et al., 2013; Brewin et al., 2015; Joshi et al., 2017b). Empirical relationships are mathematical formulations (e.g., simple or multiple regressions) that directly link water-leaving measurements to the parameter of interest in surface waters. They are simple in nature, easy to implement, and do not require deep understanding of the underlying relationships between light and water properties. Because the performance of empirical relationships is uncertain outside the range of observations that are used to develop them, their applicability is doubtful and

may cause significant errors if used in waters with different optical properties. In contrast, semi-analytical models, which are based on radiative transfer theory, invert R_{rs} using a suite of analytical and empirical relationships to derive the water IOPs (absorption and backscattering coefficients of water constituents; Lee et al., 2002). Because they solely depend on water-leaving radiance and require less information about in-water bio-optical properties, they have better applicability and accuracy compared to empirical methods in a variety of waters (IOCCG, 2006). However, a major drawback is that the retrieval of IOPs for individual water components is strongly dependent on the performance of the respective empirical models.

To some extent, this drawback is minimized in a multiband quasi-analytical algorithm (QAA) for optically deep waters (Lee et al., 2002). This algorithm analytically decomposes total non-water absorption coefficients (a_{nw}) for combined CDOM and suspended sediments (a_{dg}) and phytoplankton (a_ϕ) using their spectral information. The QAA has been improved (e.g., QAA-v5 and QAA-v6) for better performance in turbid coastal waters (Lee et al., 2009). Several studies have also contributed to the standard QAA with regional and/or global modifications in a variety of waters such as the turbid waters of the Mississippi and Atchafalaya River system (Zhu et al., 2011), coastal waters of the South China Sea (Dong et al., 2013), and inland waters of the USA and China (Li et al., 2013). A large number of studies have evaluated the standard QAA in different regions (e.g., turbid inland waters of northeast China, shallow ponds of the northwestern Mississippi, Lake Taihu, Yellow Sea, East China Sea, Arctic, and low-latitude oceans) with acceptable performance in coastal and oceanic waters, but decreasing accuracy towards CDOM-rich and sediment-rich estuarine and inland waters (Lee et al., 2010; Qing et al., 2011; Zhu et al., 2011; Mishra et al., 2013; Mitchell et al., 2014; Zheng et al., 2014; Pitarch et al., 2016). Several factors could be responsible for the QAA's poor performance in shallow waters, including the following: (1) the empirical relationships of QAA were designed using field observations in coastal and oceanic environments and may not be suitable for the optically deep estuarine and nearshore waters; and (2) a majority of empirical models of the standard QAA use R_{rs} at blue wavelengths (e.g., 443 and 490 nm). However, it is well known that satellite products suffer from large errors at short wavelengths due to uncertainties in atmospheric correction, especially in coastal waters. This suggests the need for an estuarine-specific tuning of the QAA and its evaluation and application to newer ocean color satellite sensors.

In this study, we present a tuned multiband quasi-analytical algorithm (QAA-V) that is optimized primarily for the Visible and Infrared Imaging Radiometer Suite (VIIRS) ocean color sensor and calibrated for various other ocean color sensors, such as Sentinel-3 Ocean and Land Colour Instrument (Sentinel-3 OLCI), MODerate resolution Imaging Spectroradiometer (MODIS Aqua), MEdium Res-

olution Imaging Spectroradiometer (MERIS), Sea-viewing Wide Field-of-view Sensor (SeaWiFS), and land-observing sensors, such as Landsat 8 Operational Land Imager (Landsat 8 OLI) and Sentinel-2 Multispectral Instrument (Sentinel-2 MSI), to estimate IOPs in shallow estuarine and nearshore waters. First, synthetic data were generated using Hydrolight[®] simulations (Mobley and Sundman, 2013) for highly absorbing and scattering waters and used collectively with estuarine in situ observations to update coefficients for the semi-analytical and empirical models of the standard QAA processing chain. The algorithm's performance is then evaluated on three datasets: (1) a Hydrolight-simulated dataset, (2) a subset of the well-known NASA bio-Optical Marine Algorithm Dataset (NOMAD), and (3) field observations that were obtained in various estuaries on the US East Coast and in the Gulf of Mexico. The QAA-V performance was compared to the QAA-v6, which was mainly tuned to improve QAA's performance in turbid coastal waters. Additionally, using a linear backscattering–SPM relationship, the QAA-V's applicability to VIIRS and estuarine waters is analyzed for SPM of various coastal sites, including Galveston Bay (USA). Finally, as a case study, VIIRS-derived SPM imagery of Galveston Bay was obtained following Hurricane Harvey to assess SPM dynamics in the bay and their impact on the coastal ocean.

2 Materials and methods

2.1 Data for QAA-V

Three datasets were used for tuning and evaluating QAA-V's performance in a variety of waters ranging from highly turbid estuarine environments to relatively clear shelf waters. These datasets include (1) a synthetic dataset, (2) NASA's bio-optical marine algorithm dataset, and (3) an estuarine dataset. The availability of numerous observations representing the true state of natural systems is the primary requirement for any algorithm development and validation analysis. The Hydrolight[®] radiative transfer model (Mobley and Sundman, 2013) was used to generate a large set of synthetic data (HL; $N = 561$) for tuning and extending QAA-V's ability to perform in highly absorbing and highly scattering waters (e.g., turbid estuarine environments). The process of generating synthetic data using Hydrolight[®] simulations was similar to the International Ocean-Colour Coordinating Group report (IOCCG Report 5; IOCCG, 2006) and is briefly described in Sect. S1 in the Supplement with necessary modifications based on in situ estuarine observations. The in situ estuarine and nearshore dataset (IES) included 340 concurrent water inherent optical properties (IOPs; e.g., absorption and backscattering coefficients) and above-water R_{rs} measurements at various locations on the US East Coast and in the northern Gulf of Mexico (Fig. 1a). Data were compiled from NASA's SeaBASS repository by applying a depth

threshold of 10 m for obtaining measurements in estuarine and nearshore waters (Werdell et al., 2003). The IES dataset was further divided into a training set (EcoHAB and Tampa Bay; $N = 121$) and a testing set ($N = 219$) for tuning and validating QAA-V, respectively (Table 1). NOMAD (NASA bio-Optical Marine Algorithm Dataset) is a freely available, high-quality field dataset for ocean color algorithm development and validation (Werdell and Bailey, 2005). It includes IOPs and R_{rs} collected in waters ranging from oceanic to estuarine environments, but mostly in shelf waters around the world. We extracted a subset ($N = 547$) containing complete observations of IOPs and R_{rs} (Fig. 1b). Data distributions of synthetic data clearly showed the representation of CDOM-rich and sediment-rich waters, whereas phytoplankton absorption was of secondary importance as generally observed in several estuarine environments (Fig. 2). The training and testing data (HL and IES datasets) ranged from approximately 0.1 to 7 m^{-1} for the CDOM absorption coefficient (a_{g443}), 0.05 to 4.5 m^{-1} (detritus + minerals or non-algal particles) for the absorption coefficient ($a_{\text{NAP}443}$), 0.05 to 2 m^{-1} for the phytoplankton absorption coefficient ($a_{\phi443}$), and 0.04 to 0.2 m^{-1} for the particle backscattering coefficient ($b_{\text{btmw}532}$; Fig. 2).

2.2 Data for Galveston Bay

Galveston Bay, the seventh-largest estuary in the United States (area = $\sim 1600 \text{ km}^2$; mean depth = $\sim 2 \text{ m}$), is located along the upper coast of Texas in the northern Gulf of Mexico (Fig. 1c). The Trinity River is the major source of fresh water ($\sim 50\%$) to the bay followed by the San Jacinto River ($\sim 30\%$) and local watersheds ($\sim 20\%$; Guthrie et al., 2012; Lucena and Lee, 2017). With the busiest petrochemical port in the US, Galveston Bay experiences frequent oil spills; ~ 3500 oil spill ($\sim 416\,000$ gallons) incidences were reported between 1998 and 2009 (Lester and Gonzalez, 2011). The bay is connected to the Gulf of Mexico via three passes: Bolivar Roads Pass, Rollover Pass, and San Luis Pass. Galveston Bay can be divided into four sections: (1) Trinity Bay (TB), (2) upper Galveston Bay (UGB), (3) lower Galveston Bay (LGB), and (4) East Bay (EB; Fig. 1c).

Surface water samples were collected at several stations during two field surveys on 29 September 2017 and 29–30 October 2017 as part of a larger study to investigate the aftereffects of Hurricane Harvey (25–29 August 2017) on the water quality of Galveston Bay. Available measurements of suspended particulate matter (SPM) concentration were utilized for evaluating the applicability of QAA-V in estuarine environments. Samples were filtered using precombusted and pre-weighed 47 mm , $0.7 \mu\text{m}$ porosity Whatman GF/F filters for SPM concentrations (Neukermans et al., 2012). An analytical scale with an accuracy of $\pm 0.1 \text{ mg}$ was used to measure the mass of SPM. Profiles of b_{btmw} were obtained at each station using the WETLabs VSF-3 (470, 530, 670 nm) and ECO BB (532 nm) backscattering sensors (D'Sa et al.,

Table 1. In situ estuarine and nearshore dataset (IES: IOPs and R_{rs} matchups) compiled from the SeaBASS with locations, possessing status, project instructors, and the purpose in this analysis. Apalachicola Bay, Barataria Bay, and Galveston Bay datasets were collected by the authors during various field surveys.

Experiment	Location (Depth < 10 m)	N	Processing status	Investigator(s)	Purpose for QAA-V
SWFL	Southwest Florida	5	Final	Chuanmin Hu	Validation
EcoHAB	Southwest Florida	74	Final	Kendall Carder	Tuning
Chesapeake Bay Light Tower	Chesapeake Bay	8	Preliminary	Richard Zimmermann & Glenn Cota	Validation
GEO-CAPE	Chesapeake Bay	19	Final	Richard Miller	Validation
Tampa Bay	Tampa Bay	47	Final	Chuanmin Hu	Tuning
Lake Erie	Lake Erie	3	Preliminary	Rick Gould	Validation
Horn Island	Horn Island	6	Preliminary	Bob Arnone	Validation
CoJet-4,5,6	Mobile Bay	18	Preliminary	Don Johnson	Validation
Cojet-7	Mississippi Sound	6	Preliminary	Rick Gould	Validation
BluCAR	Apalachicola Bay	32	Final	Eurico D'Sa & Christopher Osburn	Validation
BluCAR	Barataria Bay	31	Final	Eurico D'Sa & Christopher Osburn	Validation
Bio-optics	Chesapeake Bay	43	Final	Alex Gilerson	Validation
SFP	Florida Bay	8	Final	Frank Muller-Karger	Validation
Hurricane Harvey	Galveston Bay	27	Final	Eurico D'Sa & Ishan Joshi	Validation
GEOCAPE GOMEX	Northern Gulf of Mexico shelf	13	Final	Antonio Mannino & Michael Novak	Validation

2006), and surface values were averaged for depth < 1 m. Above-water measurements of water-surface radiance (L_w , $W m^{-2} nm^{-1} sr^{-1}$, nadir = 40–50°, azimuth = 90–135°), sky radiance (L_{sky} , $W m^{-2} nm^{-1} sr^{-1}$, zenith = 40–50°, azimuth = 90–135°), and reference plate radiance (L_{plate} , $W m^{-2} nm^{-1} sr^{-1}$, nadir = 0°, azimuth = 90–135°) were collected using a GER1500 512iHR spectroradiometer under clear-sky conditions (Mobley, 1999). The spectroradiometer was set to provide an average of three internal scans for considering the variability in reference and target conditions. Hence, the final spectrum was an average of nine spectra (three replicates with three internal scans per measurement) at each station (Joshi et al., 2017a). The above-water remote sensing reflectance (R_{rs}^{0+} , unit: sr^{-1}) was obtained using the following equations (Mueller et al., 2003):

$$\begin{aligned} & \text{Downwelling irradiance } (E_d) \text{ (} W m^{-2} nm^{-1} sr^{-1} \text{)} \\ & = \pi \times \frac{L_{plate}}{\rho_{plate}}, \end{aligned} \quad (1)$$

$$\begin{aligned} & \text{Above-water remote sensing reflectance } (R_{rs}^{0+}) \text{ (} sr^{-1} \text{)} \\ & = \frac{L_w - \rho \times L_{sky}}{E_d} - R_{rs} \text{ (residual)}, \end{aligned} \quad (2)$$

where ρ_{plate} is reference plate reflectance (99%) and R_{rs} (residual) is attributed to residual sky radiance, which was taken as R_{rs}^{0+} (950 nm; Mobley, 1999).

In addition, discharge data were acquired from USGS river gauge sites for the Trinity River (Romayor site USGS

08066500 and Wallisville site USGS 08067252) and at the San Jacinto River (the eastern flank USGS 8070200 and the western flank USGS 8068090) for examining variations in freshwater flows after Hurricane Harvey. Wind speed and direction were acquired from NOAA Eagle Point station (ID-8771013) in Galveston Bay. Level-1 VIIRS (nine images) and MODIS Aqua (one image) products were obtained from NASA's Ocean Color data archive (OBPG, NASA), including three images during field surveys in Galveston Bay. VIIRS imagery was not available on 29 September 2017 corresponding to the first field survey; hence, the next-day image (30 September 2017) was used in this analysis. The Sentinel-3 OLCI Level-2 image was downloaded from the Earth Observation Portal (EUMETSAT) and the Landsat 8 OLI Level-1 image was downloaded from the USGS Earth Explorer for 29 October 2017.

2.3 QAA processing chain

The underlying structure of QAA-V is similar to the standard quasi-analytical algorithm (QAA; Lee et al., 2002) and its modifications (e.g., QAA-v5 and QAA-v6) suitable to coastal and open oceans (Lee et al., 2007, 2009). The processing pathway of QAA-V is illustrated in Table 2 and briefly mentioned here with justifications for necessary modifications. The QAA and its updated versions rely upon the principle that the spectral remote sensing reflectance just below the water surface (R_{rs}^{0-}) is a function of the spectral

Table 2. Processing steps of QAA-V for obtaining total absorption (a_t) and backscattering coefficients (b_{bt}). Levels 0 and 1C were adopted from Lee et al. (2002), whereas 1A and 1B were modified in this study*. Level 1C1 is adopted from D'Sa et al. (2007).

Level	Parameter	Model	Type
0	$R_{rs}^{0-}(\lambda)$	$R_{rs}^{0-}(\lambda) = \frac{R_{rs}^{0+}(\lambda)}{0.52+0.17 \times R_{rs}^{0+}(\lambda)}$	Semi-analytical
1A	$u(\lambda)$	$u(\lambda) = \frac{-g_0 + [g_0^2 + 4 \times g_1 \times R_{rs}^{0-}(\lambda)]^{0.5}}{2 \times g_1}$ $\rho = \log_{10} \left(\frac{R_{rs}^{0-}(\lambda_0)}{R_{rs}^{0-}(671)} \right)$ $g_0 = 0.0788$ and $g_1 = 0.2379$ for $\rho < 0.25$ $g_0 = 0.0895$ and $g_1 = 0.1247$ for $\rho \geq 0.25$	Semi-analytical
1B	$a_{tnw}(\lambda_0)$ $\lambda_0 = 551$ or 555 $\lambda_1 = 671$	$a_{tnw}(\lambda_0) = \begin{cases} 10^{(0.139 - 1.788 \times \rho + 0.490 \times \rho^2)} & \text{if } \rho < 0.25 \\ 10^{(0.406 - 2.940 \times \rho + 0.928 \times \rho^2)} & \text{if } \rho \geq 0.25 \end{cases}$ $\rho = \log_{10} \left(\frac{R_{rs}^{0-}(\lambda_0)}{R_{rs}^{0-}(\lambda_1)} \right)$	Empirical
1C 0	$b_{btmw}(\lambda_0)$	$b_{btmw}(\lambda_0) = \frac{(a_{tnw}(\lambda_0) + a_w(\lambda_0)) \times u(\lambda_0)}{1 - u(\lambda_0)} - b_{bw}(\lambda_0)$	Analytical
1	η	$\eta = -0.566 - 1.395 \times \log_{10}(b_{btmw}555)$	Empirical
2	$b_{bt}(\lambda)$	$b_{bt}(\lambda) = b_{bw}(\lambda) + b_{btmw}(\lambda_0) \times \left(\frac{\lambda_0}{\lambda} \right)^\eta$	Semi-analytical
3	$a_t(\lambda)$	$a_t(\lambda) = b_{bt}(\lambda) \times \left(\frac{1 - u(\lambda)}{u(\lambda)} \right)$	Analytical
SPM models			
	This study	$SPM = (103.07 \times b_{btmw}532) + 0.24$	Empirical
	D'Sa et al. (2007)	$SPM = (106.93 \times b_{btmw}555) + 0.61$	Empirical
	Nechad et al. (2010)	$SPM = \left(\frac{A^\rho \times \rho_w}{1 - \rho_w / C^\rho} \right) + B^\rho$; where $A^\rho = 373.79 \text{ mg L}^{-1}$, $B^\rho = 1.47 \text{ mg L}^{-1}$, $C^\rho = 0.1747$ for $\lambda = 670 \text{ nm}$	Empirical

* Parameters $g_0 = 0.0788$ and $g_1 = 0.2379$ were derived with HL datasets. $\lambda_0 = 551$ or 555 nm ; R_{rs}^{0-} : remote sensing reflectance just below water surface; a_{tnw} : total non-water absorption coefficient; b_{btmw} : total non-water backscattering coefficient; a_w : water absorption coefficient; b_{bw} : water backscattering coefficient; η : power-law exponent (D'Sa et al., 2007); SPM: suspended particulate matter concentration. Note: in the SPM model comparison, input backscattering values are obtained from QAA-V, whereas surface reflectance (ρ) is obtained by multiplying π and above-surface remote sensing reflectance (R_{rs}^{0+}).

backscattering and absorption coefficients (Gordon et al., 1988), and it can be modeled using the following equation (Table 2, Level 1A):

$$R_{rs}^{0-}(\lambda) \text{ (sr}^{-1}\text{)} = g_0 \times u(\lambda) + g_1 \times [u(\lambda)]^2,$$

$$u(\lambda) = \frac{b_{bt}(\lambda)}{a_t(\lambda) + b_{bt}(\lambda)}, \tag{3}$$

where a_t and b_{bt} are the total absorption coefficient and total backscattering coefficient (m^{-1}), respectively. R_{rs}^{0-} can be easily computed from above-surface remote sensing reflectance (R_{rs}^{0+}) using the following relationship (Lee et al., 1999; Table 2, Level 0).

$$R_{rs}^{0-}(\lambda) \text{ (sr}^{-1}\text{)} = \frac{R_{rs}^{0+}(\lambda)}{(0.52 + 1.7 \times R_{rs}^{0+}(\lambda))} \tag{4}$$

The coefficients g_0 and g_1 are empirically derived parameters related to the directional nature of the upwelling light field

(Q) and f (well known as the f/Q term). These coefficients depend on sun angle, viewing geometry, wind speed, and the bio-optical state of natural waters and vary with phase function (Morel and Gentili, 1991, 1993, 1996). Thus, appropriate coefficients are needed for different aquatic environments (Lee et al., 2002). For example, the values of g_0 and g_1 were previously suggested as 0.0949 and 0.0794, respectively, for oceanic waters (Gordon et al., 1988). Later, better approximations of g_0 (0.0895) and g_1 (0.1247) were proposed for reflective coastal waters using radiative transfer models on simulated data (Lee et al., 1999). Average values of g_0 and g_1 from Gordon et al. (1988) and Lee et al. (1999) were also used for both coastal and oceanic waters (Lee et al., 1999). The synthetic data for obtaining these historic values of g_0 and g_1 were generated using case-1 radiative transfer models. As the first modification, we updated these coefficients using Hydrolight® simulations with a four-

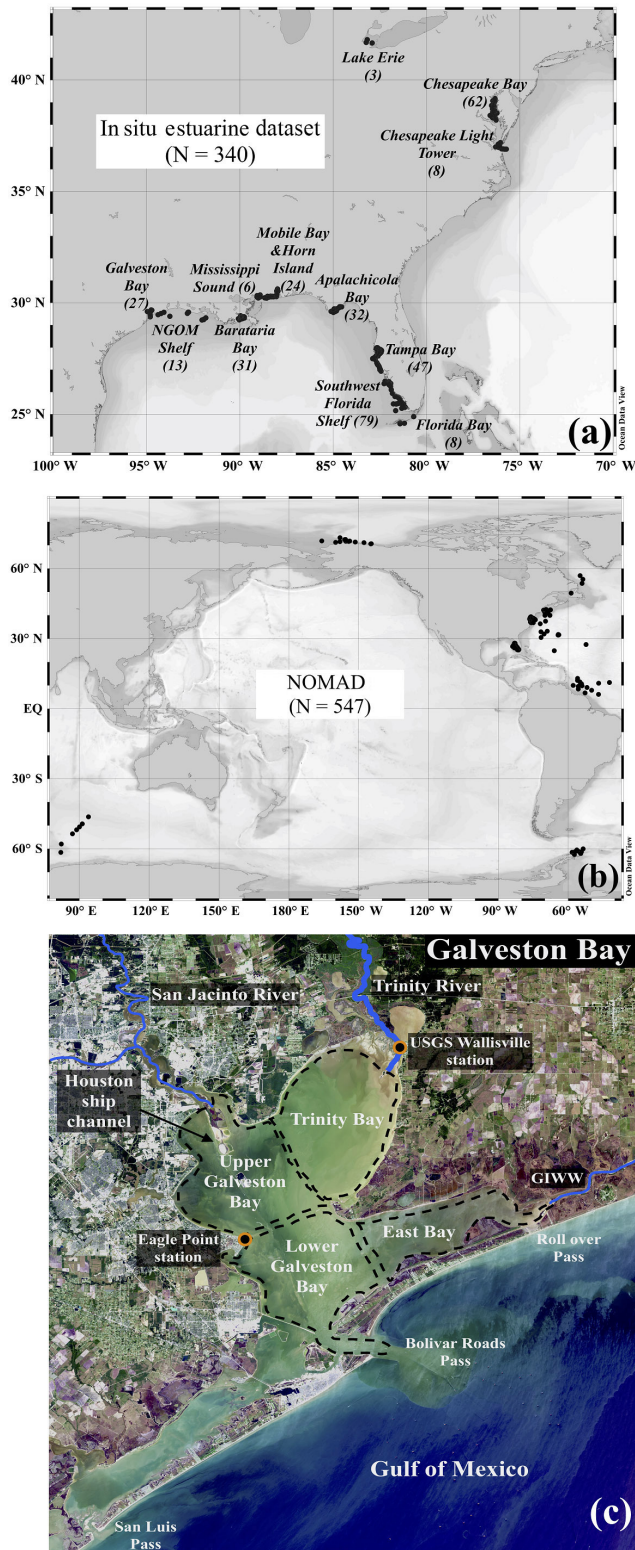


Figure 1. (a) In situ dataset (IES) representing estuarine and nearshore waters (< 10 m) on the US East Coast and in the northern Gulf of Mexico ($N = 340$), (b) NOMAD ($N = 547$), and (c) Galveston Bay, Texas (USA). GIWW: Gulf Intracoastal Waterway.

component case-2 model (Sect. S1) because a shallow water environment was the main focus of this study. In addition, it has been previously suggested that molecular scattering may primarily contribute to R_{rs} , especially in the blue and green wavelengths in oceanic waters. However, the phase function effect of water molecules could be much smaller than that of particles in nearshore and estuarine waters. Hence, we have avoided separating Eq. (3) as is usually done to account for the phase function effects of individual backscattering contributors (Lee et al., 2013; Zheng et al., 2014).

Next, QAA-v6 uses a set of empirical models (e.g., Eq. 5) based on above-surface R_{rs} threshold (0.0015 sr^{-1}) to estimate the total non-water absorption coefficient at a reference wavelength in coastal and oceanic waters (Table 2, Level 1B):

if $R_{rs}^{0+}(670) < 0.0015 \text{ sr}^{-1}$

$$a_{\text{tnw}}(\lambda_0) = 10^{(-1.146 - 1.366 \times x - 0.469 \times x^2)},$$

$$\text{where } x = \log_{10} \left(\frac{R_{rs}^{0-}(443) + R_{rs}^{0-}(490)}{R_{rs}^{0-}(\lambda_0) + 5 \times R_{rs}^{0-}(670) \times \frac{R_{rs}^{0-}(670)}{R_{rs}^{0-}(490)}} \right),$$

$$\text{otherwise, } a_{\text{tnw}}(\lambda_1) = 0.39 \times \left[\frac{R_{rs}^{0+}(670)}{R_{rs}^{0+}(443) + R_{rs}^{0+}(490)} \right]^{1.14}, \quad (5)$$

where a_{tnw} is the total non-water absorption coefficient (m^{-1}), $\lambda_0 = 555$, and $\lambda_1 = 670$ nm.

We avoided using blue wavelengths in our empirical models as blue bands, especially 443 nm or lower, suffer from large errors in atmospheric correction due to the high abundance of CDOM, suspended particles, and absorbing aerosols in a coastal environment. In contrast, the green to red band ratio (GRBR) can be used for estimating the absorption coefficient of an individual water constituent with the primary condition of their dominance in the study region. The GRBR has been used, for example, to monitor water constituents in various estuarine and coastal waters, e.g., a_{g355} in Barataria Bay, USA (Joshi and D'Sa, 2015), a_{g412} in Apalachicola Bay, USA (Joshi et al., 2017a), a_{dg412} in Galveston Bay, USA (D'Sa et al., 2018), suspended particulate matter (D'Sa et al., 2007), and chlorophyll index (harmful algal bloom) in the northern Gulf of Mexico (Qi et al., 2015). Estuarine waters are generally characterized by a high abundance of CDOM, mineral particles, or both and are thus known to have strong light absorption towards shorter wavelengths, sometimes even in the green region. In contrast, the light absorption in the red region usually remains minimal for CDOM and mineral particles. As a result, the green band can be considered as a pilot band to capture variations in dissolved or mineral particle absorption, whereas the red band is a reference band. Hence, small variations in the GRBR are suitable to capture large variations in absorption at shorter wavelengths due to the exponential nature of CDOM and particle absorption. A similar band ratio (RGCI; red to green chlorophyll index) has been used in

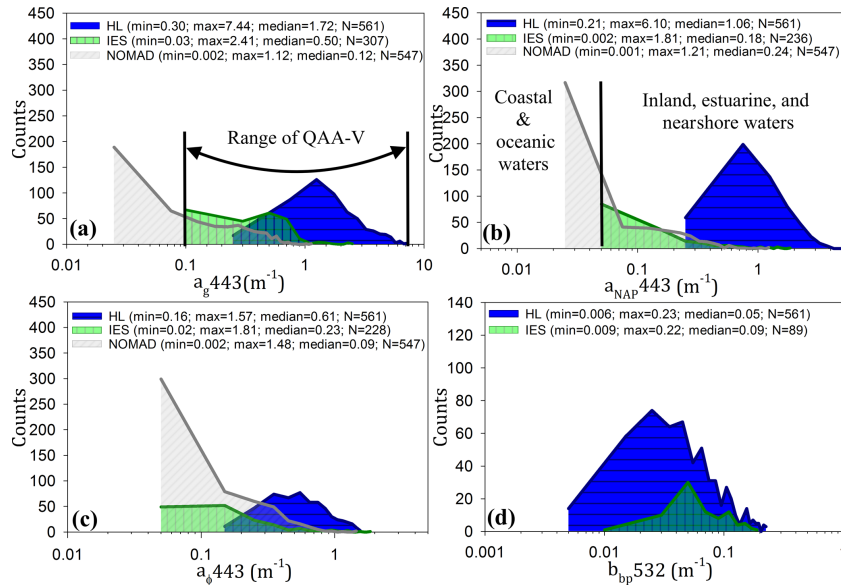


Figure 2. Data statistics and distribution of water IOPs, (a) a_g443 , (b) a_{NAP443} , (c) $a_{\phi443}$, and (d) b_{bt532} for synthetic data (HL, Hydrolight[®]; blue), in situ estuarine and nearshore data (IES; green), and the NOMAD (grey). The range of QAA-V indicates data that are used to update QAA-V for shallow waters (e.g., HL and IES).

a semi-analytical approach to obtain chlorophyll-*a* concentrations for estimating phytoplankton absorption $a_{\phi670}$ and subsequently a_{tw670} in the productive waters of Tampa Bay, USA (Le et al., 2013). The red to green band ratio (RGR) works well to quantify variations in chlorophyll concentrations, especially in phytoplankton-dominated waters. Therefore, the RGR (or RGBR) can be overall associated with the dominant water constituent in the study area. However, optically active water constituents collectively contribute to total light absorption, and hence these band ratios can also be used for the remote estimation of a_{tw} at green wavelengths, especially in estuarine waters where variations in total absorption coefficients are often noticeable due to a high abundance of one or more (e.g., CDOM and particles) water components. A ratio of R_{rs} at the red and green wavelengths (e.g., 640/645 and 555 nm for MODIS) was previously used in the standard QAA to improve the estimates of a_{tw} at a reference wavelength (e.g., 555 nm for MODIS) in turbid waters, which worked reasonably in coastal waters (Lee et al., 2002; Chen and Zhang, 2015). The processing of the high-spatial-resolution I-1 band (640 nm; spatial resolution: 375 m) is not supported by NASA's SeaDAS tool; therefore, our analysis was limited to the available ocean color bands (M1 to M5; spatial resolution: 750 m).

Additionally, the selection of the reference wavelength in Eq. (5) is another important factor affecting the retrieval of IOPs in QAA. The use of a reference wavelength at red wavelengths (e.g., > 600 nm) was suggested for relatively turbid coastal waters where particulate and dissolved absorption is much lower than water absorption (Lee et al., 2002; Aurin and Dierssen, 2012). We used 555 nm as a reference wave-

length for three reasons: (1) there is a lack of absorption measurements at red wavelengths (e.g., IES dataset) to tune empirical models (Table 2, Level 1B); (2) the use of a red reference wavelength would likely deteriorate the estimations in blue wavelengths due to errors in spectral extrapolation corresponding to the empirical nature of the backscattering power-law exponent, η ; and (3) a strong relationship between the green to red band ratio and total non-water absorption at 555 nm is observed in this study.

Once $u(\lambda_0)$ is obtained as the positive root of Eq. (3) using R_{rs}^{0-} and the coefficients g_0 and g_1 , the backscattering coefficient at a reference wavelength ($b_{btw}(\lambda_0)$) can be easily obtained with $u(\lambda_0)$, $a_{tw}(\lambda_0)$, and the following analytical model (Table 2, Level 1C0):

$$b_{btw}(\lambda_0) \text{ (m}^{-1}\text{)} = \left(\frac{u(\lambda_0)}{1 - u(\lambda_0)} \right) \times (a_{tw}(\lambda_0) + a_w(\lambda_0)) - b_{bw}(\lambda_0), \tag{6}$$

where a_w and b_{bw} are water absorption and backscattering coefficients, respectively. The spectral distribution of the particulate backscattering coefficient (b_{btw}) can be modeled using the power-law model (Lee et al., 2002; Table 2, Level 1C2):

$$b_{bt}(\lambda) \text{ (m}^{-1}\text{)} = b_{bw}(\lambda) + b_{btw}(\lambda_0) \times \left(\frac{\lambda_0}{\lambda} \right)^\eta, \tag{7}$$

where η is the spectral shape of b_{btw} distribution. The standard QAA-v6 uses the following empirical model to obtain η .

Table 3. The calibration coefficients for sensor-specific QAA tuning. λ_0 is a sensor-specific reference wavelength.

Sensor	$\rho = \log_{10} \left(\frac{R_{rs}^{0-}(\lambda_0)}{R_{rs}} \right)^{0-} (\lambda_1)$	$a_{\text{tnw}}(\lambda_0) = 10^{(a+b\rho+c\rho^2)}$					
		(Level 1B, Table 2)					
		$\rho < 0.25$			$\rho \geq 0.25$ and $\rho \leq 0.65$		
		<i>a</i>	<i>b</i>	<i>c</i>	<i>a</i>	<i>b</i>	<i>c</i>
VIIRS	$\lambda_0 = 551 \text{ nm} \ \& \ \lambda_1 = 671 \text{ nm}$	0.139	-1.788	0.490	0.406	-2.940	0.928
MODIS Aqua	$\lambda_0 = 555 \text{ nm} \ \& \ \lambda_1 = 667 \text{ nm}$	0.091	-1.800	0.560	0.275	-2.674	0.813
Sentinel-3 OLCI	$\lambda_0 = 560 \text{ nm} \ \& \ \lambda_1 = 674 \text{ nm}$	0.176	-1.830	0.528	0.397	2.940	0.800
MERIS	$\lambda_0 = 560 \text{ nm} \ \& \ \lambda_1 = 665 \text{ nm}$	0.081	-1.868	0.688	0.314	-2.733	0.713
SeaWiFS	$\lambda_0 = 555 \text{ nm} \ \& \ \lambda_1 = 670 \text{ nm}$	0.128	-1.792	0.505	0.276	-2.742	0.842
Sentinel-2 MSI	$\lambda_0 = 560 \text{ nm (band 3) \ \&}$ $\lambda_1 = 665 \text{ nm (band 4)}$	0.0814	-1.868	0.688	0.223	-2.732	0.740
Landsat 8 OLI	$\lambda_0 = 560 \text{ nm (band 3) \ \&}$ $\lambda_1 = 655 \text{ nm (band 4)}$	-0.087	-1.900	0.952	0.057	-2.667	0.753

$$\eta = 2 \times \left(1 - 1.2 \times e^{\left(-0.9 \times \frac{R_{rs}^{0-}(443)}{R_{rs}^{0-}(555)} \right)} \right) \quad (8)$$

The variation in the power-law exponent η depends on water properties and the size of particles according to Mie theory and it is extremely difficult to retrieve η from R_{rs} in nearshore waters (Aurin and Dierssen, 2012). Thus, we adopted a different approach of obtaining η from $b_{\text{btw}555}$ with a linear relationship that was formulated using field observations in the turbid waters near the Mississippi River delta (D'Sa et al., 2007; Table 2, Level 1C1).

$$\eta = -0.566 - 1.395 \times \log_{10}(b_{\text{btw}555}) \quad (9)$$

The spectral distribution of total absorption coefficients was then obtained using b_{btw} and u (Table 2, Level 1C3).

$$a_t(\lambda) \text{ (m}^{-1}\text{)} = \left(\frac{1-u(\lambda)}{u(\lambda)} \right) \times b_{\text{bt}}(\lambda) \quad (10)$$

To extend and evaluate the applicability of estuarine-specific QAA tuning, it was further applied to various ocean color (Sentinel-3 OLCI, MODIS Aqua, MERIS, and SeaWiFS) and land-observing sensors (Landsat 8 OLI and Sentinel-2 MSI). The calibration coefficients for obtaining the total non-water absorption coefficient at a reference wavelength ($a_{\text{tnw}}(\lambda_0)$; Level 1B in Table 2) are given in Table 3.

2.4 Atmospheric correction of satellite imagery

Level-1 satellite imagery was corrected for the atmosphere using the SeaDAS 7.4 image processing tool as described previously (Joshi et al., 2017a), and mean values of a 3×3 pixel box centered at a station location were considered as reasonable satellite matchups for the field measurements.

In addition, in situ R_{rs} values were matched to the central wavelengths of spectral bands using the spectral response functions of respective satellite sensors prior to the sensor-specific tuning and validation:

$$R_{\text{rsRSR}} \text{ (sr}^{-1}\text{)} = \frac{\int_{\lambda_1}^{\lambda_2} \text{RSR}(\lambda) \times R_{\text{rsinsitu}}(\lambda) d\lambda}{\int_{\lambda_1}^{\lambda_2} \text{RSR}(\lambda) d\lambda}, \quad (11)$$

where RSR is the relative spectral response for the satellite sensor, λ_1 is the lower bound of a spectral band, and λ_2 is the upper bound of a spectral band.

An iterative NIR atmospheric correction scheme was previously evaluated for estuarine environments (Bailey et al., 2010; Werdell et al., 2010; Joshi et al., 2017a); however, it yielded negative R_{rs} at blue wavelengths and atmospheric correction failure at several pixels in Galveston Bay. In comparison, the errors in atmospheric correction were considerably reduced with the MUMM NIR correction as it was designed for low to moderately turbid waters (Ruddick et al., 2006; Novoa et al., 2017). Furthermore, the validation of atmospheric-corrected VIIRS imagery showed reasonable performance of the MUMM atmospheric correction scheme during both field campaigns in Galveston Bay (Table 4). The MRE, which was relatively higher at the blue wavelengths, was greatly reduced towards the green and red wavelengths. Thus, the success of the atmospheric correction procedure was decided based on the green and red bands, since only these bands were used to tune QAA in this study. However, the observed large errors at other wavelengths (e.g., blue bands) were likely due to the high abundance of CDOM and particles in the study region and the aerosol model selection in the atmospheric correction procedure (Minu et al., 2014). The time difference between field and satellite measurements resulted in an error enhancement at longer wavelengths with relatively smaller errors in October (difference of 0 days) and larger errors in September (difference of +1 days; Table 4).

Table 4. The performance evaluation of the atmospheric correction procedure (MUMM) in Galveston Bay (USA) during two field campaigns (29 September and 29–30 October 2017). The MRE remained relatively lower than the blue for the green and red bands (bold fonts).

Image date	Difference of days for field observation	Number of stations	Absolute mean relative error (MRE; %)					
			410 nm	443 nm	486 nm	551 nm	671 nm	All bands
30 Sep 2017	+1	9	114.7	40.5	19.8	10.9	18.1	40.8
29 Oct 2017	0	10	55.8	12.4	5.1	6.3	8.9	17.7
30 Oct 2017	0	7	139.6	42.1	21.5	7.5	7.6	43.7

Overall, low MRE in the green and red wavelengths indicated the usefulness of the MUMM atmospheric correction for investigating bio-optical properties with the QAA-V processing chain and VIIRS ocean color data in Galveston Bay (USA).

2.5 Statistical analysis

The algorithm's performance and atmospheric-corrected VIIRS imagery were evaluated using coefficients of determination (R^2), root mean square error ($RMSE_{\log 10}$), bias ($Bias_{\log 10}$), and absolute mean relative error (MRE).

$$Bias_{\log 10} = \frac{1}{n} \times \sum_{i=1}^n [\log_{10}(y_i) - \log_{10}(x_i)] \quad (12)$$

$$RMSE_{\log 10} = \sqrt{\frac{1}{n} \times \sum_{i=1}^n [\log_{10}(y_i) - \log_{10}(x_i)]^2} \quad (13)$$

$$MRE (\%) = \frac{100}{n} \times \sum_{i=1}^n \left[\left| \frac{y_i - x_i}{x_i} \right| \right] \quad (14)$$

R software was used to generate synthetic IOPs for the Hydrolight[®] case-2 model and the statistical analysis presented in this study.

3 Results

3.1 Modifications to standard QAA

A new set of g_0 (0.0788) and g_1 (0.2379) obtained using Hydrolight-simulated IOPs and R_{rs} is proposed for the highly attenuating waters of this study. These coefficients showed a notable departure from the quadratic relationship, especially in highly scattering waters when compared to Gordon et al. (1988) and Lee et al. (1999, 2002; Fig. 3a). We used the historical values g_0 (0.0895) and g_1 (0.1245) for less reflective nearshore and shelf waters (i.e., threshold $\rho \geq 0.25$) in the validation analysis (Fig. 3b). Overall, the threshold-based selection of the u vs. R_{rs}^{0-} model showed a valid retrieval of u ($\approx b_{bt}/(a_t + b_{bt})$) as seen when u was analytically used to obtain the total absorption coefficient (a_{t555}) and the total backscattering coefficients (b_{bt555} ; HL dataset) and vice versa (Fig. 4a, b; Table 2, Level 1A).

The performance of QAA-V was largely dependent on the estimation of the total non-water absorption coefficient (a_{tnw}) in Level 1B (Table 2). In this study, the empirical model of standard QAA-v6 (Eq. 5) was replaced by a tuned empirical power-law relationship using a training set (IES; $N = 121$; Table 1) of in situ observations and Hydrolight[®] synthetic data (HL; $N = 561$):

$$a_{tnw}(\lambda_0) = \begin{cases} 10^{(0.139 - 1.788 \times \rho + 0.490 \times \rho^2)} & \text{if } \rho < 0.25 \\ 10^{(0.406 - 2.940 \times \rho + 0.928 \times \rho^2)} & \text{if } \rho \geq 0.25 \end{cases},$$

$$\rho = \log_{10} \left(\frac{R_{rs}^{0-}(\lambda_0)}{R_{rs}^{0-}(\lambda_1)} \right), \quad (15)$$

where a_{tnw} is the total non-water absorption coefficient, $\lambda_0 = 551$ or 555 nm, and $\lambda_1 = 671$ nm.

A threshold value of 0.25 was set for ρ to merge the HL and IES datasets excluding the NOMAD (Fig. 3b). The a_{tnw555} ($\rho > 1.0$) nearly reached the lower limit close to zero for oceanic waters, likely due to low concentrations of reflecting and absorbing materials. Thus, we suggest the upper threshold of $\rho = 0.65$ beyond which Level 1B fails and overestimates water $a_{tnw}(\lambda_0)$. Likewise, negative ρ values of synthetic data represented CDOM-rich waters with very strong absorption even at green wavelengths (e.g., 555 nm). For HL data, the modeled a_{tnw555} showed a reasonable performance of the green to red band ratio model (MRE = 16.3 %, $bias_{\log 10} = -0.0208$, $RMSE_{\log 10} = 0.0963 \text{ m}^{-1}$, $N = 561$; Fig. 4c). The performance of the empirical model, however, showed a significant difference within the IES training data ($R^2 = 0.90$, MRE = 21 %, $bias_{\log 10} = -0.0015$, $RMSE_{\log 10} = 0.12 \text{ m}^{-1}$, $N = 120$) and testing data ($R^2 = 0.72$, MRE = 34 %, $bias_{\log 10} = -0.0294$, $RMSE_{\log 10} = 0.19 \text{ m}^{-1}$, $N = 209$; Fig. 4d).

3.2 Comparison of QAA-V with the standard QAA-v6

The QAA-v6 algorithm was applied separately on HL synthetic data and IES field observations for a direct comparison with QAA-V in retrieving optical properties in estuarine waters. Figure 4e shows the performance of QAA-v6 in estimating the total non-water absorption coefficient at 555 nm (a_{tnw555}) with HL synthetic data. In comparison to QAA-V, the QAA-v6 showed an obvious underestima-

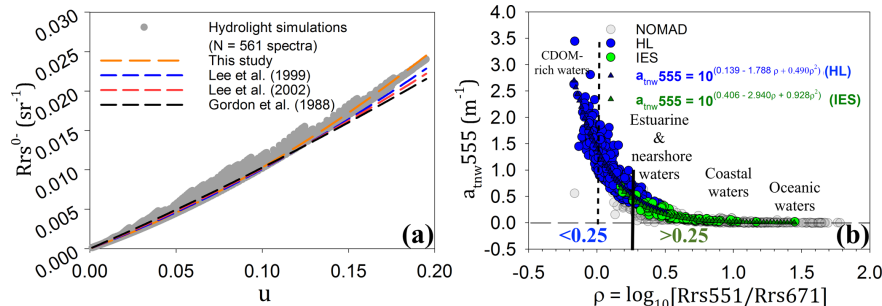


Figure 3. (a) $u (= b_b/(a + b_b))$ vs. R_{rs}^{0-} for various studies (this study: orange; Lee et al., 1999: blue; Lee et al., 2002: red; Gordon et al., 1988: black) using HL datasets. (b) The relationship between green to red band ratio and $a_{tnw,555}$ for different datasets (HL: blue, IES: green, NOMAD: grey). Black line shows a threshold to facilitate a smooth transition from in situ to synthetic data in modeling $a_{tnw,555}$. A dashed line separates data with negative ρ .

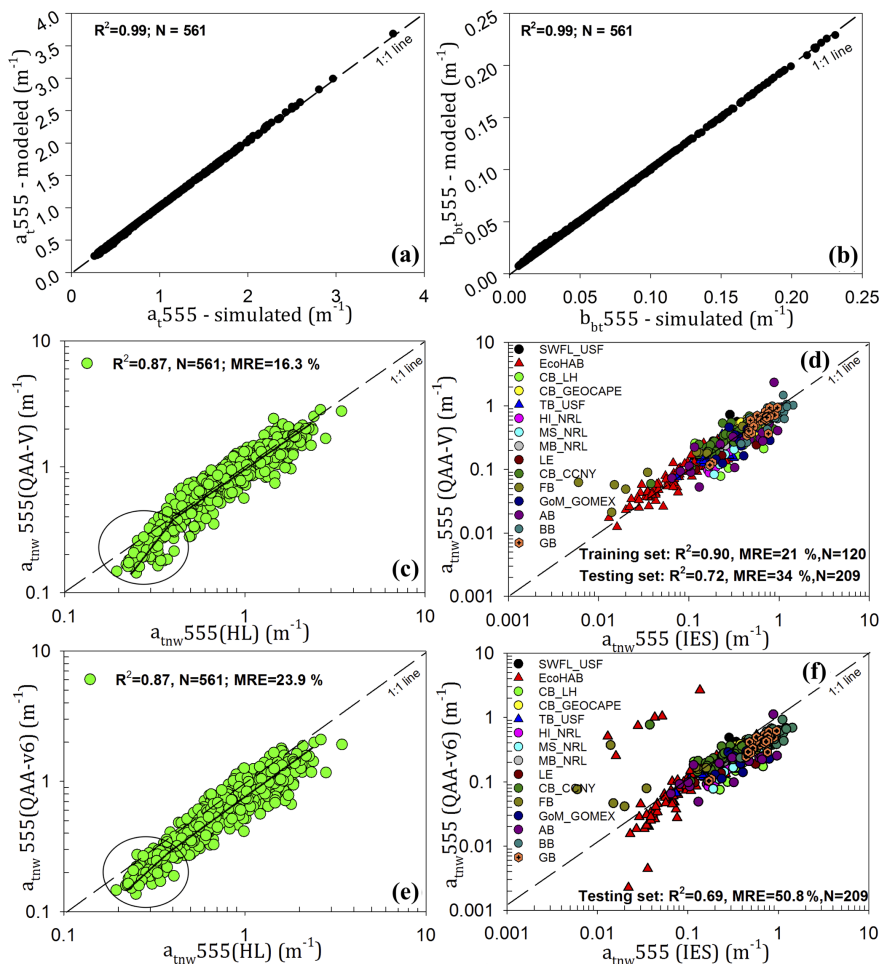


Figure 4. Validation of R_{rs}^{0-} vs. u model using HL data for (a) $a_{t,555}$ and (b) $b_{bt,555}$. Validation of QAA-V-modeled $a_{tnw,555}$ with “true” $a_{tnw,555}$ for (c) the HL synthetic dataset (bias_{log10} = -0.0208, RMSE_{log10} = 0.0963 m⁻¹) and (d) IES dataset (bias_{log10} = -0.0294, RMSE_{log10} = 0.190 m⁻¹). Validation of QAA-v6-modeled $a_{tnw,555}$ with “true” $a_{tnw,555}$ for (e) the HL synthetic dataset (bias_{log10} = -0.1180, RMSE_{log10} = 0.1490 m⁻¹) and (f) IES dataset (bias_{log10} = -0.1252, RMSE_{log10} = 0.278 m⁻¹). Note: the training set includes EcoHAB and Tampa Bay data (Table 1). IOP measurements of Galveston Bay (this study) are shown with orange hexagons. MRE: absolute mean relative error (%). TB: Tampa Bay, AB: Apalachicola Bay, BB: Barataria Bay, CB: Chesapeake Bay, FB: Florida Bay, GoM: Gulf of Mexico, HI: Horn Island, LE: Lake Erie, MS: Mississippi Sound, MB: Mobile Bay, SWFL: southwest Florida, GB: Galveston Bay (Table 1).

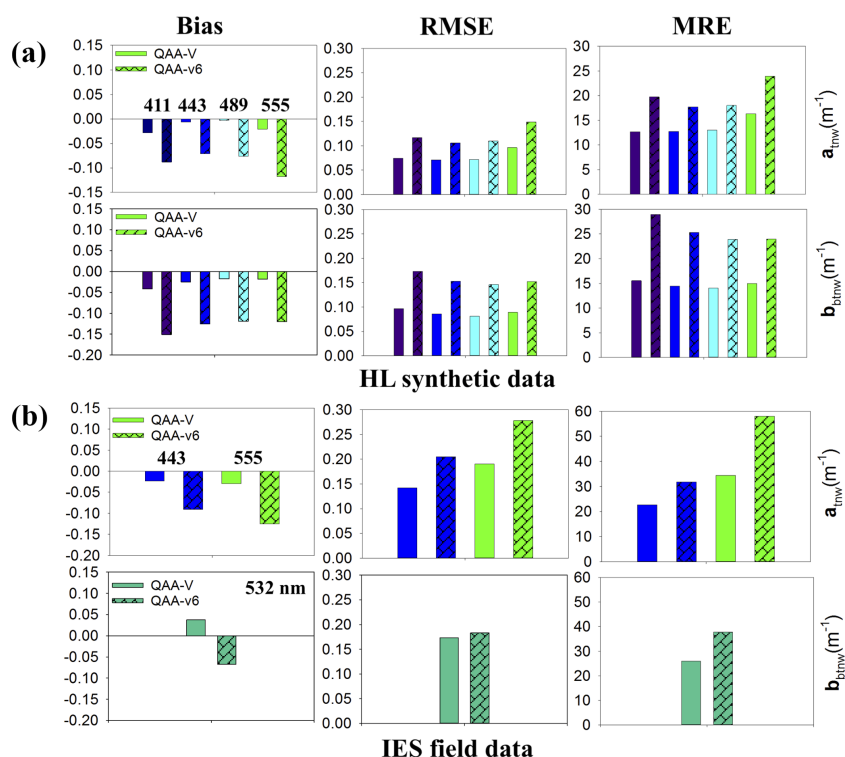


Figure 5. Statistical assessment of QAA-V in comparison to QAA-v6 (updated on May 2015) using synthetic data (HL; **a**) and estuarine and nearshore field data (IES; **b**). Color scheme indicates a_{tnw} and b_{btnw} at 411 nm (dark blue), 443 nm (blue), 489 nm (cyan), 555 nm (green), and 532 nm (dark green) wavelengths. MRE: absolute mean relative error (%). RMSE and bias are in m^{-1} .

tion at 555 nm, especially for $a_{tnw555} > \sim 0.3 m^{-1}$. Statistical assessment showed that QAA-V is more accurate than the QAA-v6 with approximately 83 % less bias, 35 % decreased RMSE, and 1.5-fold lower MRE (Fig. 5, Sect. S2). For IES data, the QAA-v6 showed a clear difference with a poor performance at several stations (Fig. 4f) compared to QAA-V (Fig. 4d). Furthermore, the retrieval errors were large towards the upper and lower ends (e.g., $a_{tnw555} > \sim 0.3$ and $< \sim 0.1 m^{-1}$). Overall, the QAA-v6 had an obvious underestimation with approximately 75 % greater bias, 31 % increased RMSE, and 2-fold higher MRE than the QAA-V at 555 nm (Fig. 5, Sect. S2).

3.3 Evaluation of QAA-V on synthetic HL data, NOMAD, and IES data

Hydrolight-simulated case-2 water R_{rs}^{0+} spectra were fed into QAA-V to derive a_{tnw} and b_{btnw} at 411, 443, 489, and 555 nm (Fig. 6). Although a negative bias indicated an overall underestimation of modeled absorption coefficient at 555 nm (Fig. 4c), QAA-V performed satisfactorily in the blue region (Fig. 6a). Furthermore, the modeled a_{tnw} at blue wavelengths showed relatively lower MRE $< 13\%$ and $RMSE_{\log 10} < 0.075 m^{-1}$ despite the errors in modeled a_{tnw555} at values less than $0.3 m^{-1}$ (relatively low CDOM and mineral particle abundance), indicating the secondary

importance of the green reference wavelengths in transferring errors to blue wavelengths in QAA-V's processing chain compared to the red reference wavelengths (Aurin and Dierssen, 2012). Similarly, QAA-V also estimated b_{btnw} with MRE $< 16\%$ at four wavelengths (Fig. 6b). When compared to the QAA-v6, QAA-V performed with approximately 80–90 % lower bias, 30–40 % reduced RMSE, and 1–2-fold decreased MRE at blue wavelengths (Fig. 5, Sect. S2). QAA-V's performance on the standard NOMAD showed that the MRE was $< 30\%$ for all blue wavelengths with a_{tnw443} being the best-retrieved parameter ($R^2 = 0.94$, MRE = 24.3 %, $N = 547$). However, large errors were observed for $a_{tnw} < 0.1 m^{-1}$ at all wavelengths (Fig. 7a).

For field validation, R_{rs}^{0+} spectra from 15 experiments of IES data were fed into QAA-V for obtaining a_{tnw443} and $b_{btnw532}$ (Fig. 7b and c; Table 1). Modeled IOPs showed overall good results for a_{tnw443} (MRE = 15 % for training data and 23 % for testing data; Fig. 7b) and $b_{btnw532}$ (MRE = 32 % for all data and 26 % for all data except Apalachicola Bay; Fig. 7c). A further analysis of individual datasets showed noticeable variations in MRE. For example, MRE varied from ~ 11 –24 % among the five best-performing datasets for estimating a_{tnw443} , whereas it varied from ~ 40 –75 % for three poorly performing datasets with preliminary processing status (Table 1). On the IES data,

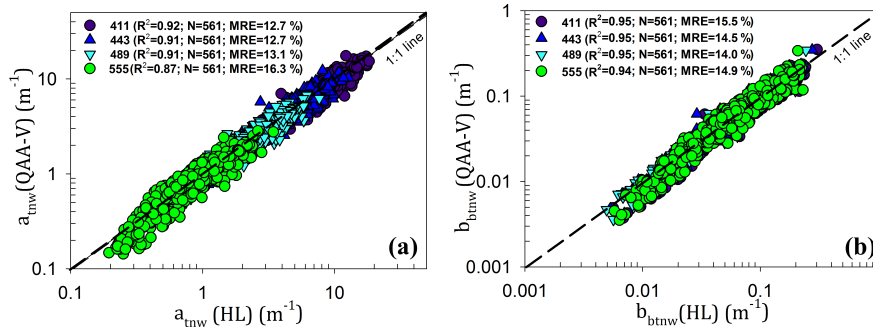


Figure 6. Validation of QAA-V on synthetic data (HL) for (a) a_{tnw} and (b) b_{btnw} at 411 nm (dark blue), 443 nm (blue), 489 nm (cyan), and 555 nm (green) wavelengths. MRE: absolute mean relative error (%).

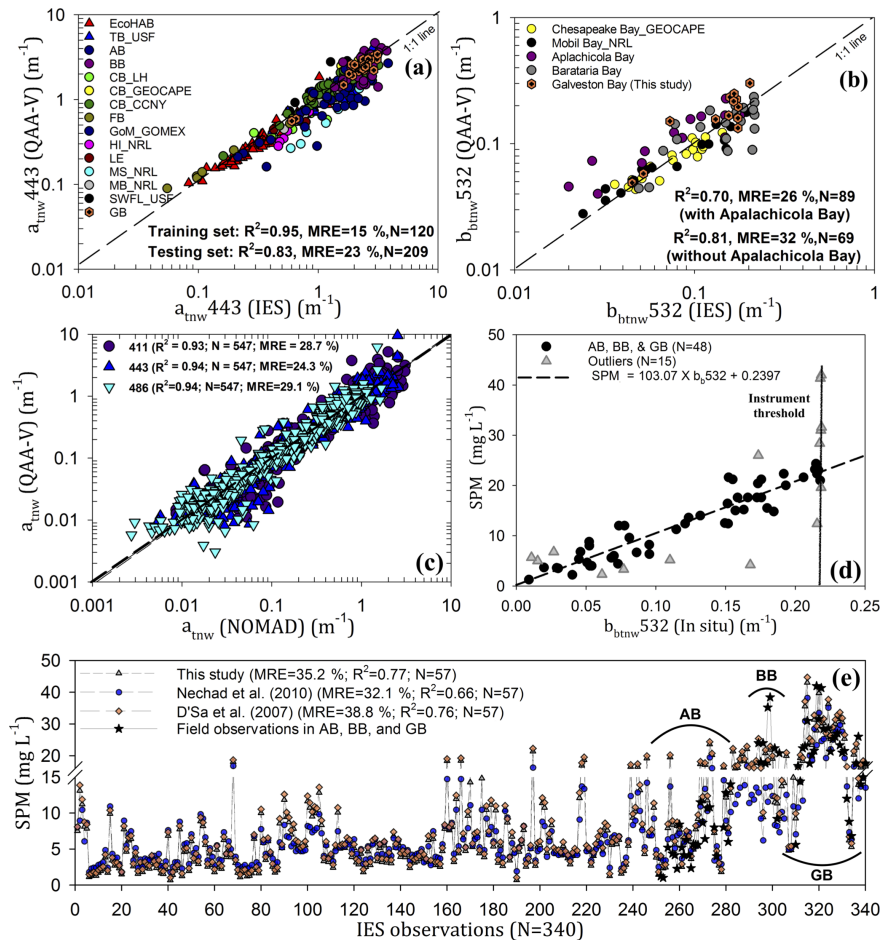


Figure 7. Evaluation of QAA-V's performance on the estuarine and nearshore dataset (IES) for (a) $a_{\text{tnw}443}$ and (b) $b_{\text{btnw}532}$ and on the NOMADs for (c) a_{tnw} at 411 nm (dark blue), 443 nm (blue), and 488 nm (cyan) wavelengths. (d) SPM– $b_{\text{btnw}532}$ relationship ($R^2 = 0.89$ without outliers) that was formulated based on field observations in Apalachicola Bay, Barataria Bay, and Galveston Bay. (e) A comparison of the SPM– $b_{\text{btnw}532}$ relationship in this study (grey triangles) with SPM models from Nechad et al. (2010; blue circles) and D'Sa et al. (2007; orange squares) and with field observations in AB, BB, and GB (black stars). TB: Tampa Bay, AB: Apalachicola Bay, BB: Barataria Bay, CB: Chesapeake Bay, FB: Florida Bay, GoM: Gulf of Mexico, HI: Horn Island, LE: Lake Erie, MS: Mississippi Sound, MB: Mobile Bay, SWFL: southwest Florida, GB: Galveston Bay (Table 1). Training set includes EcoHAB and Tampa Bay datasets. MRE: absolute mean relative error (%).

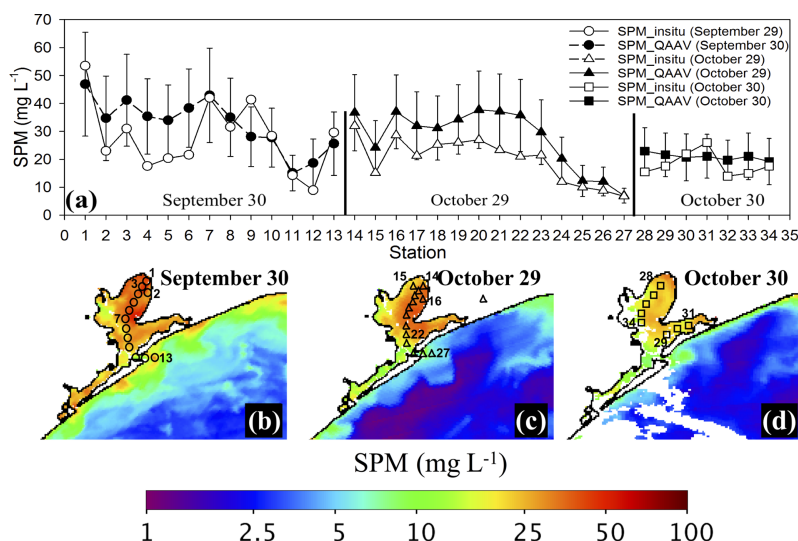


Figure 8. (a) Validation of QAA-V-derived SPM vs. in situ SPM for (b) 30 September 2017 (MRE = 39.9 %, $N = 13$), (c) 29 October 2017 (MRE = 39.1 %, $N = 14$), and (d) 30 October 2017 (MRE = 26.6 %, $N = 7$). Stations for validation analysis (Fig. 8a) are also illustrated in corresponding SPM maps.

QAA-V showed fewer errors in retrieving water IOPs than QAA-v6 (Fig. 5, Sect. S2).

3.4 SPM- $b_{\text{btw}532}$ relationship and validation

A linear relationship ($R^2 = 0.89$; $N = 33$) was observed between $b_{\text{btw}532}$ and SPM (Eq. 16; Fig. 7d). It was used for evaluating the applicability of QAA-V to generate synoptic maps of SPM using the VIIRS ocean color sensor in estuarine environments.

$$\text{SPM} = 103.07 \times (b_{\text{btw}532}) + 0.24; \text{ where } b_{\text{btw}532} = \text{backscattering coefficient at 532 nm} \quad (16)$$

It is important to note that the backscattering sensor had an upper threshold of 0.23 m^{-1} at which the sensor saturated and failed to detect variability in SPM; however, the linearity in the SPM- $b_{\text{btw}532}$ relationship was assumed beyond the threshold (0.23 m^{-1}) in this study. The SPM- $b_{\text{btw}532}$ relationship was compared to a similar relationship developed in turbid coastal waters of the Mississippi River (D'Sa et al., 2007) and a generic multisensor algorithm (Nechad et al., 2010) using the IES dataset (Fig. 7e; Table 2). The three algorithms showed quite similar trends despite different water properties of the IES dataset. When compared to field observations of SPM in Apalachicola Bay, Barataria Bay, and Galveston Bay, these algorithms showed good performance with the lowest error for the single-wavelength generic algorithm of Nechad et al. (2010; MRE = 32.1 %, $N = 57$) and the highest error for the SPM- $b_{\text{btw}555}$ relationship of D'Sa et al. (2007; MRE = 38.8 %, $N = 57$; Fig. 7e).

3.5 Evaluation of QAA-V in a turbid estuarine environment

The SPM- $b_{\text{btw}532}$ relationship in this study was applied to VIIRS imagery for evaluating satellite-based application of QAA-V in a turbid estuarine environment (Fig. 8). The regional SPM- $b_{\text{btw}532}$ relationship showed $\sim 35\%$ overall MRE in a satellite-field comparison (Fig. 8a) for Galveston Bay during the two field campaigns (Fig. 8b-d). Both field and estimated SPM concentrations followed a similar pattern of high to low values along the north-to-south transect. A large-to-small error trend from 30 September (MRE = 39.9 %) to 30 October (MRE = 26.6 %) was similar to the error trend in the atmospheric correction of the VIIRS imagery (Table 4). Based on these results, a sequence of cloud-free and atmospherically corrected VIIRS imagery was converted to SPM maps using the QAA-V processing chain (Table 2) for analyzing post-hurricane SPM dynamics in Galveston Bay (Fig. 9).

3.6 Extending the QAA-V tuning to various satellite sensors

The estuarine-specific green to red band tuning was further applied to evaluate and extend its applicability to past and present ocean color (e.g., SeaWiFS, MERIS, MODIS Aqua, and Sentinel-3 OLCI) and land-observing sensors (Landsat 8 OLI and Sentinel-2 MSI; Table 3). The validation analysis showed a promising performance of QAA-V tuning in obtaining the total non-water absorption coefficient ($a_{\text{tnw}443}$) and total-non water backscattering coefficient ($b_{\text{btw}470}$) in the optically complex and shallow waters of Galveston Bay (Fig. 10). Overall, different satellite sensors showed simi-

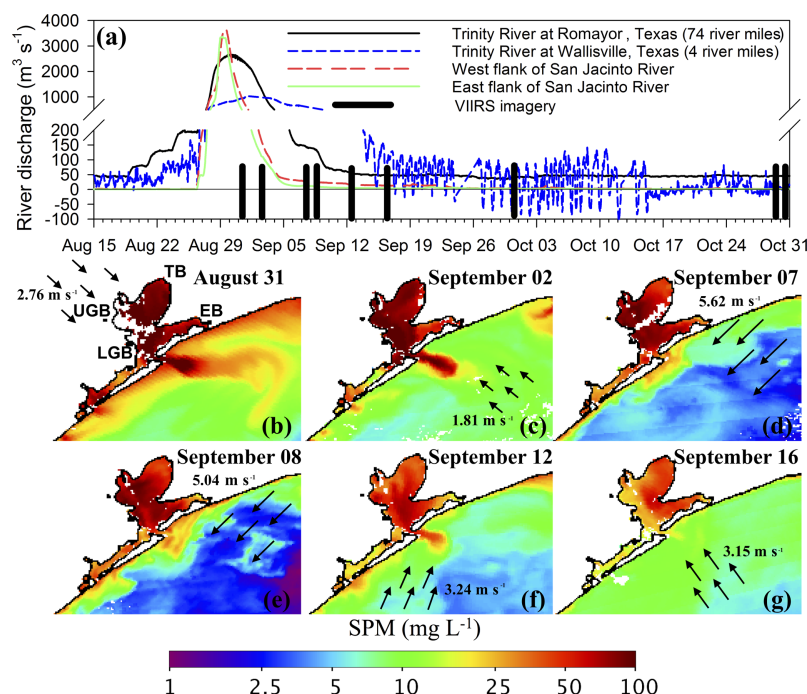


Figure 9. (a) River discharge of the Trinity River at Romayor, Texas (black line) and Wallisville, Texas (blue line); the west flank of the San Jacinto River (red line) and the east flank of the San Jacinto River (green line). The river discharge at the Wallisville site was not corrected for the tides. Black bars represent the days of VIIRS satellite imagery for SPM analysis in Galveston Bay. (b–g) Post-hurricane SPM maps of Galveston Bay. TB: Trinity Bay, UGB: upper Galveston Bay, LGB: lower Galveston Bay, EB: East Bay (Fig. 1c).

lar trends of $a_{\text{tnw}443}$ and $b_{\text{btw}470}$ along the transect despite having different spectral and spatial sensor resolutions (Fig. 10I–IV). The MREs were ~ 15 , 9, and 12% for $a_{\text{tnw}443}$ retrievals from VIIRS, MODIS A, and Sentinel-3 OLCI sensors, respectively (Fig. 10a–c and I), whereas they were ~ 26 , 7, and 22% for $b_{\text{btw}470}$ retrievals on 29 October 2017 (Fig. 10f–h and III). For Landsat 8 OLI, the MREs were ~ 20 and $\sim 10\%$ for $a_{\text{tnw}443}$ and $b_{\text{btw}470}$, respectively, on 29 September 2017 (Fig. 10e, j, II, IV).

4 Discussion

4.1 QAA-V

The standard QAA (Lee et al., 2002) was first tuned with VIIRS sensor bands as QAA-V and then extended to other satellite sensors to obtain more accurate estimates of water IOPs (e.g., total absorption and backscattering coefficients) in shallow estuarine and nearshore waters. For this purpose, two modifications were applied to the QAA: (1) the coefficients g_0 and g_1 of a quadratic model were updated using Hydrolight[®] simulations for highly absorbing and highly scattering waters (Eq. 3, Fig. 3a); and (2) an empirical model of QAA for obtaining the total absorption coefficient at a reference wavelength was replaced by a set of empirical models that were optimized for highly attenuating estuarine and

nearshore waters (Eq. 15, Fig. 3b). The validity of these modifications is demonstrated in Fig. 4. The updated coefficients, g_0 and g_1 , showed a significant departure from historical values (Gordon et al., 1998; Lee et al., 1999, 2002) especially at green and red wavelengths in highly attenuating waters. Likewise, these coefficients were updated using a synthetic dataset representing highly attenuating waters and they may not perform satisfactorily in less reflective nearshore and coastal environments. This limitation was addressed by adopting a water-type switching of the u vs. R_{rs}^{0-} algorithm based on a green to red band ratio threshold (ρ) in the QAA-V processing chain (Table 2). The effectiveness of tuning g_0 and g_1 is also supported by a previous study showing an approximate 5-fold bias reduction in obtaining total non-water IOPs at 440 nm (Aurin and Dierssen, 2012).

Overall, the negative bias for the HL datasets indicated that the threshold-based empirical models underestimated $a_{\text{tnw}555}$; however, a major error in the model performance was observed at the lower end of the absorption of values, likely for two reasons: (1) the failure of the threshold (ρ) in providing a smooth switching of empirical relationships between the highly absorbing and scattering waters (synthetic HL dataset) and estuarine and nearshore waters (IES dataset; Fig. 4b); and (2) the unsuitability of the empirical relationship for some R_{rs} spectra in the HL synthetic data based on the green to red band ratio (e.g., $a_{\text{tnw}555} < 0.3 \text{ m}^{-1}$; Fig. 4a). In contrast, both empirical relationships worked reasonably

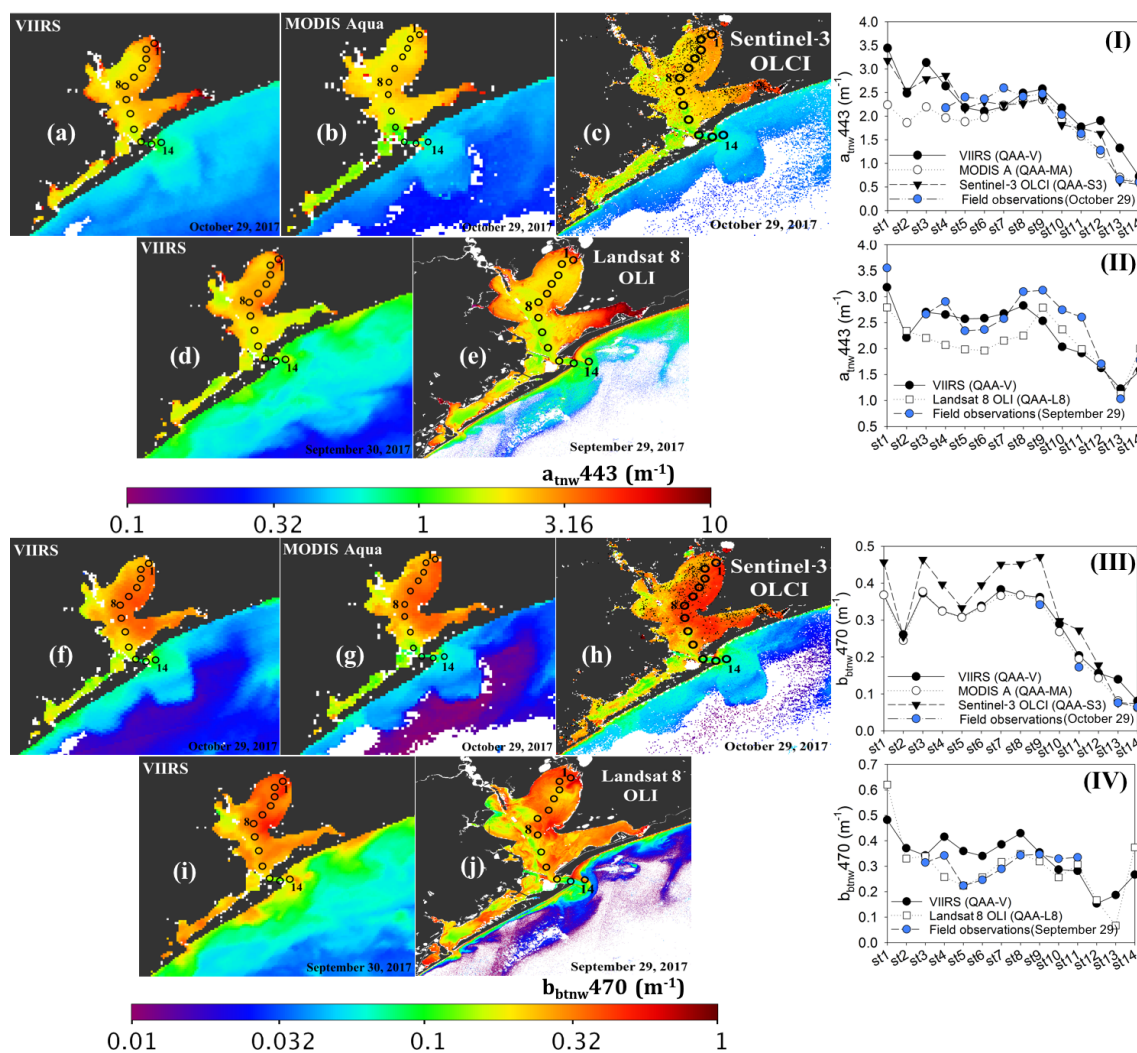


Figure 10. Application of sensor-specific QAA-V tuning to obtain maps of $a_{\text{tnw}443}$ using (a) VIIRS, (b) MODIS Aqua, and (c) Sentinel-3 OLCI on 29 October 2017 and (d) VIIRS and (e) Landsat 8 OLI on 30 September and 29 September 2017, respectively. The validation of these maps with the field observations along the transect (St. 1 to St. 14) is shown in (I) for Fig. 8a–c and in (II) for Fig. 8d and e. The maps of $b_{\text{btwn}470}$ were obtained similarly for (f) VIIRS (29 October 2017), (g) MODIS Aqua, (h) Sentinel-3 OLCI, (i) VIIRS (30 September 2017), and (j) Landsat 8 OLI (29 September 2017) with their validation results in (III) and (IV). Parameter values beyond the upper limit of tuned QAA ($\rho > 0.65$) are shown masked in white.

well in providing a smooth transition from nearshore waters to the highly turbid and highly absorbing waters of the IES data (Fig. 4b). However, the large differences within an IES dataset (e.g., training data and test data) could be explained by the processing status of different individual experiments in the IES dataset (Table 1). Training data included R_{rs} measurements in the final processing status from two well-known experiments, namely the EcoHAB ($N = 74$) and Tampa Bay monitoring programs ($N = 47$; Table 1). Individual absolute mean relative errors (MREs) for these data are 24 and 16%, respectively. In contrast, few datasets used in the testing set were in the preliminary processing stage with $\text{MRE} > 35\%$ (e.g., Chesapeake Bay Light Tower, Horn Island, Cojet 7, and Lake Erie).

The validation of QAA-V in a variety of waters yielded reasonable performance as shown in Figs. 6 and 7. For the HL dataset, an error difference ($\sim 2\%$) between a_{tnw} (Fig. 6a) and b_{btwn} (Fig. 6b) could be associated with errors in Levels 0 and 1A of the QAA processing chain (Table 2). The effect of this systematic error ($\sim 1\text{--}2\%$) is also present in the estimates of backscattering coefficients at blue wavelengths; this could be due to uncertainties in various parameters of the semi-analytical power-law model such as the power-law exponent η (Table 2; Level 1C1). It has previously been shown that η is important for obtaining b_{bt} and its tuning can be responsible for an approximate 4-fold decrease in the percentage difference for $b_{\text{bt}440}$ in estuarine waters over QAA's η model (Eq. 8; Aurin and Dierssen, 2012). As

we used a linear model based on $b_{\text{btw}}(\lambda_0)$ for η (D'Sa et al., 2007), the modeled backscattering coefficient may suffer from errors due to uncertainties in the empirical estimation of the power-law exponent. η does not play any role in retrieving $b_{\text{btw}}(\lambda_0)$, and hence errors associated with η should not affect modeled $b_{\text{btw}}(\lambda_0)$. However, the errors in η may affect the retrieval of b_{btw} at other wavelengths (e.g., $b_{\text{btw}470}$; Table 2). For the NOMAD, the observed large MRE in relatively clearer waters ($a_{\text{tnw}} < 0.1 \text{ m}^{-1}$) can be due to the fact that the empirical relationships for modeling $a_{\text{tnw}}(\lambda_0)$ were not designed to work with very low values of non-water absorption coefficients, as generally observed in shelf and oceanic environments (Fig. 7a; Eq. 5). For the IES datasets, the retrieval of $a_{\text{tnw}443}$ is obviously improved compared to $a_{\text{tnw}555}$ (Figs. 4d and 7b); however, a 1- to 2-fold increase in errors is observed in IOP retrieval when QAA-V is applied to the field data in contrast to synthetic data. This error enhancement can be due to several factors, including (1) failure to achieve a smooth switching between highly absorbing and reflecting waters and estuarine and nearshore waters in real data (Fig. 4a), (2) inclusion of preliminary data in validation analysis (Table 1), (3) the uncertainty propagation of the previous levels of the QAA-V processing chain (e.g., errors in various empirical, semi-analytical, and analytical relationships; Table 2), and (4) the difference in methodology of data collection, raw data processing, instrumentation, and measurement and instrument errors. For example, reflectance measurements, the primary input of QAA-V, can have large errors if measured in turbid waters and with large viewing angles (Lee et al., 1999), while bottom contamination may introduce an additional error since in situ data represent shallow water environments. The bottom effect could probably be reduced with sophisticated correction schemes (Lee et al., 1998, 1999; Li et al., 2017).

A statistical comparison showed that the QAA-V provided better estimations of IOPs than the standard QAA-v6 in estuarine and nearshore waters (Fig. 5). Also, a green to red band ratio is better suited for the satellite application of QAA in shallow waters due to fewer errors in these bands (Table 4). In contrast, several studies have demonstrated an overestimation in blue bands in turbid waters, likely due to errors in the atmospheric correction (Joshi et al., 2017a; Chen and Zhang, 2015, and reference therein). This overestimation could lead to the observed underestimation of $a_{\text{tnw}555}$ and subsequently the underestimation of a and b_b at different wavelengths in lower levels of the QAA processing chain (Fig. 5, Table 2).

4.2 The SPM optical model

Traditionally, suspended particulate matter (SPM) has been retrieved from remote sensing imagery using single or multi-band empirical relationships between above-surface R_{rs} and SPM concentrations (Doxaran et al., 2002; Miller and McKee, 2004; D'Sa et al., 2007; Han et al., 2016). While empirical relationships are easy to implement, they are regionally

limited and may cause large errors if applied to different waters due to differences in particle properties such as absorption, particle size and composition, and refractive index. Furthermore, above-surface R_{rs} , even at the red and NIR wavelengths at which particle attenuation controls the R_{rs} signal, is not a “true” representation of particles as the R_{rs} signal is also marginally contributed to by the absorption of water and other optically active materials. Hence, this approach has a limitation as it can have robust performance only in particle-dominated waters. Another way to estimate SPM concentration is to relate it to particle backscattering coefficients (b_{bp}). Several studies have reported the efficacy of this approach in estimating concentrations of total suspended material (TSM) and particulate organic carbon (POC) in a variety of waters ranging from estuarine to open oceans (Stramski et al., 1999; Loisel et al., 2001; Aurin and Dierssen, 2012).

When the SPM– $b_{\text{btw}532}$ relationship was applied to the VIIRS imagery, both field- and satellite-estimated SPM concentrations showed a similar pattern of high to low along a north-to-south transect in Galveston Bay; however, the differences remained elevated in the turbid region of Trinity Bay (St. 2 to St. 6 in Fig. 8b and St. 16 to St. 23 in Fig. 8c). Factors contributing to these differences include (1) the error propagation from various steps of the QAA-V processing chain to $b_{\text{btw}532}$ (e.g., 20–30 %, Fig. 7c) and hence further down to the SPM inversion, (2) the uncertainty in the atmospheric-corrected green and red R_{rs} (e.g., 5–20 %, Table 4), (3) the uncertainty in the SPM– $b_{\text{btw}532}$ relationship due to limited observations, (4) the assumption of linearity in the SPM– $b_{\text{btw}532}$ model beyond the instrument threshold, which may not hold well because the $b_{\text{btw}532}$ to SPM ratio depends on the particle nature and it may not always be constant, especially in highly turbid waters, and (5) errors in SPM measurements. For example, SPM is usually measured with a $0.7 \mu\text{m}$ (average pore size) GF/F filter, which only represents the total concentration of particles greater than this size. However, while smaller particles may not have significant contributions to the mass-specific property of SPM (e.g., concentration), particles smaller than this size can contribute notably to the underestimation of SPM concentrations in highly turbid waters (Sect. S3). Furthermore, small particles and even colloidal particles ($< 0.2 \mu\text{m}$) are known to contribute significantly to total particle backscattering in coastal waters (Zhang and Gray, 2015; Zhang et al., 2011). For instance, high winds associated with the passage of a cold front on 28 October 2017 (not shown) could have resulted in the resuspension of smaller particles at the shallower stations on 29 October (Fig. 8c) and contributed to greater differences between satellite estimates and field SPM measurements. Interestingly, on the following day (30 October) under calmer conditions, the differences reduced substantially (Fig. 8d). Thus, the mismatch between mass-specific and optical properties could be a major source of error in the SPM– $b_{\text{btw}532}$ relationship and hence the observed difference in field–satellite matchups.

4.3 Satellite application of QAA-V to Galveston Bay: post-Hurricane Harvey SPM dynamics

A sequence of SPM maps derived from VIIRS imagery using QAA-V revealed interesting patterns of SPM concentrations in Galveston Bay following Hurricane Harvey (Figs. 8 and 9). Hurricane Harvey, a category 4 hurricane, caused catastrophic flooding in the Houston metropolitan area and the surrounding regions of Galveston's Bay drainage basin with great potential to degrade the bay's water quality.

The dramatic increase in the discharge of water from the Trinity and San Jacinto rivers into Galveston Bay (Fig. 9a) following the record rainfall and flooding associated with Hurricane Harvey reveals different patterns of discharge, with the San Jacinto River peaking and retreating to pre-hurricane levels much quicker than the Trinity River. This reflects the differences of the two river basins, as well as the intensity and variability of the precipitation associated with the hurricane in the two basins. A sequence of post-hurricane SPM maps of Galveston Bay (Fig. 9b–g) reveals distinct spatial and temporal patterns of SPM variations within and outside the bay, including the offshore shelf waters that appeared to be strongly influenced by the river discharge and wind forcing. The immediate effect of Hurricane Harvey was clearly evident on 31 August when unusually high SPM concentrations ($> 75 \text{ mg L}^{-1}$) were observed throughout the bay corresponding to high freshwater inputs from the Trinity and the San Jacinto rivers into Galveston Bay (Fig. 9a and b). The SPM-rich plume ($> 75 \text{ mg L}^{-1}$) extended from the Bolivar Roads Pass to a large region of the coastal and shelf waters. In contrast, the bay experienced elevated SPM concentrations on 2 September, but the plume was limited by wind forcing and a reduction in fresh water to the bay (Fig. 9a and c).

The strong northeasterly winds ($\sim 5\text{--}6 \text{ m s}^{-1}$) observed on 7 and 8 September appeared to restrict the SPM plume closer to the bay entrance and the inner shelf waters (Fig. 9d and e). Despite the reduced freshwater inflow into the upper Galveston Bay, sustained freshwater inputs from the Trinity River ($\sim 500 \text{ m}^3 \text{ s}^{-1}$) and strong northeasterly winds (e.g., sediment resuspension) could have resulted in elevated SPM concentrations throughout the bay. Furthermore, wind-induced downwelling currents appeared to transport low SPM offshore waters nearshore, while the high SPM nearshore and plume waters were likely downwelled and could have eventually settled into the shelf sediments.

Despite the noticeable reduction in the Trinity River flow, SPM concentrations remained high within the bay on 12 September, indicating the importance of wind-induced sediment resuspension for SPM dynamics in the shallow water environments. However, outside the bay, a well-defined and elevated SPM plume extended offshore, likely associated with the southwesterly winds, which induced the offshore transport of the inner shelf waters (Fig. 9f). On 16 September, total freshwater inflow to Galveston Bay was reduced significantly (~ 500 to $\sim 100 \text{ m}^3 \text{ s}^{-1}$ in the Trinity River) with SPM

generally reduced throughout the bay. However, Trinity Bay and East Bay showed relatively higher SPM than the upper and lower Galveston Bay (Fig. 9g), likely due to a more delayed discharge through the Trinity River and the wetlands.

Overall, the QAA-V-based SPM maps of Galveston Bay showed distinct variations in SPM concentrations following Hurricane Harvey. Although the Trinity Bay and the upper Galveston Bay responded similarly a few days following the hurricane, distinct SPM patterns emerged (e.g., lower SPM in the western and higher in the eastern part of the bay) after 2 weeks, suggesting different influences in the eastern and western parts of the bay. For example, floodwaters from the Houston metropolitan and surrounding region appeared to have receded within a few days of the hurricane event (Fig. 9a), whereas the discharge of floodwaters was elevated through the Trinity River over the course of several weeks after Hurricane Harvey. These floodwaters could have accumulated first in wetlands and numerous water bodies in the eastern region and lower Trinity basin during the hurricane event and eventually emptied to the main Trinity River channel. SPM was also elevated in the East Bay, but concentrations were generally lower within the first 2 weeks, suggesting this region of the bay mostly remained isolated from the other regions of Galveston Bay. Nonetheless, this region receives discharge from the surrounding wetlands, which could have been elevated during this period. Overall, wind forcing was also important in controlling the extent and the dispersal of the sediment-rich plume waters into the shelf and in contributing to the SPM variability within the bay due to sediment resuspension and its transport into the shelf waters.

4.4 Application of the QAA tuning to various ocean color and land-observing sensors

Sensor-specific QAA tuning (e.g., QAA-V for VIIRS, MODIS, Landsat 8 OLI, and Sentinel-3 OLCI) showed an overall valid retrieval of absorption and backscattering coefficients with various ocean color and land observation sensors (Fig. 10). Although satellite-derived values and trends of $a_{\text{tnw}443}$ and $b_{\text{btw}470}$ are similar to the field observations, the observed discrepancies could, in addition to the uncertainties in field measurements, be due to several sources of errors. For example, it is well known that satellite products suffer from large errors in the blue region, especially in coastal waters due to atmospheric correction (Table 4; Sect. S4). The large errors between field- and Landsat-8-OLI-derived $a_{\text{tnw}443}$ could have been due to the fact that the QAA processing chain uses these erroneous blue R_{rs} values to obtain a_{tnw} at blue wavelengths (Table 2; Level 3). However, the b_{btw} retrievals at blue wavelengths are unaffected by the blue R_{rs} inputs (Table 2; Level 2). Likewise, the errors were relatively smaller at the reference wavelength (Table 4) because the proposed QAA tuning avoided using blue wavelengths in the primary step of getting a_{tnw} and b_{btw} at a reference wavelength. Hence, the atmospheric correction proce-

ture is an important step that would impact the performance of QAA-V in ocean color applications of shallow estuarine and nearshore waters.

Another important discrepancy among various sensor maps is the number of masked pixels in shelf waters (Fig. 10). We have used a VIIRS band-ratio-based threshold ($\rho = 0.65$) to separate green waters (e.g., productive coastal waters) and blue waters (e.g., open ocean; Eq. 15) and applied it to various satellite sensors. Although this threshold worked well for the sensors with similar green and red bands (e.g., MODIS A and VIIRS), it did not perform as well for Sentinel-3 OLCI and Landsat 8 OLI because of notable differences between the green and red bands of these sensors and the VIIRS sensor (Table 3). Thus, while the proposed threshold works well to represent estuarine and nearshore waters for various ocean color and land-observing sensors, it could be further optimized for each satellite sensor.

5 Conclusions

A multiband quasi-analytical algorithm tuned for the VIIRS ocean color sensor (QAA-V) and for estuarine and nearshore waters was proposed. Two major changes were applied to the standard QAA (Lee et al., 2002): (1) the coefficients g_0 and g_1 of a semi-analytical quadratic relationship were updated to obtain u from the R_{rs} (Eq. 1), and (2) a threshold-based empirical model was proposed using the green to red band ratio (GRBR) to estimate the total absorption coefficient at a reference wavelength. The QAA-V-derived total absorption and backscattering coefficients showed a good relationship in a variety of waters ranging from highly turbid and highly absorbing (MRE < 17 %) to relatively clearer coastal waters (MRE < 30 %). Moreover, a reasonable performance (MRE < 25 %) using in situ estuarine and nearshore data indicated the usefulness of the GRBR in modeling total absorption coefficients in estuarine waters regardless of the dominance of one or more water constituents (e.g., CDOM, mineral particles, or phytoplankton). This band ratio needs to be explored further for various ocean color sensors and in different estuarine and nearshore environments around the world. The QAA-V may not perform satisfactorily in optically shallow waters as the empirical relationships were designed specifically for optically deep environments. This study showed good retrieval of backscattering coefficients (MRE = ~ 25–30 %); however, the errors increased towards the lower levels of the QAA-V processing chain (e.g., MRE = ~ 35 % in estimating SPM), likely due to the lack of b_{btw} –SPM matchups in a variety of waters in formulating a robust SPM– b_{btw} relationship corresponding to estuarine waters. This limitation suggests a great need for in situ backscattering measurements in various shallow environments and their availability for public use.

The QAA-V and a regional SPM– b_{btw} relationship were applied to a sequence of VIIRS imagery for investigat-

ing post-hurricane SPM dynamics in Galveston Bay. Despite noticeable errors, especially in turbid regions of the bay, the application of QAA-V showed great potential in revealing the SPM patterns due to post-hurricane variations linked to freshwater inflow to the bay and wind forcing. A sequence of SPM maps after the passage of Hurricane Harvey showed that Galveston Bay received massive amounts of SPM due to large volumes of freshwater input from the two major rivers and the surrounding regions. However, while the freshwater inflow reduced within a few days in the western part of the bay, it remained high over the course of several weeks in the eastern part of the bay, providing evidence of the short-term storage capacity of wetlands and numerous freshwater reservoirs in the lower Trinity basin. This discharge pattern coupled with different residence times in the western and eastern parts of the bay resulted in distinct SPM patterns in the two regions of the bay. Furthermore, while winds appeared to have played an important role in resuspending sediments within the bay, they were critical in the transport and dispersion of sediments into the shelf waters of the Gulf of Mexico.

This study did not address bottom reflectance effects (e.g., during clear-water conditions), Raman scattering, and chlorophyll fluorescence that may have degraded the QAA-V's performance. Furthermore, the tuning of the semi-analytical and empirical relationships (e.g., η in Table 2) was not possible due to scarcity of field IOPs (e.g., backscattering measurements). Although further refinements and validation studies are necessary to improve the performance and applicability of QAA-V in spatially and temporally distinct shallow waters around the world, the promising results of this study suggest that the application of QAA-V to various ocean color and land observation satellites can be a useful tool to assess the bio-optical state and water quality dynamics in a variety of coastal systems around the world.

Data availability. Data from field measurements are available upon request from the corresponding author.

Supplement. The supplement related to this article is available online at: <https://doi.org/10.5194/bg-15-4065-2018-supplement>.

Author contributions. IJ and ED conceived and designed the research; IJ analyzed the data and both authors contributed to writing the paper.

Competing interests. The authors declare that they have no conflict of interest.

Acknowledgements. We thank the NASA Ocean Color Biology Processing Group (OBGP) for providing access to the VIIRS ocean color data. We also acknowledge NASA OBGP for SeaBASS data repository and individual project PIs who made their bio-optical observations available for public use. We thank USGS and NOAA for providing various meteorological and hydrological data to support this work. The authors acknowledge NASA funding through grant no. 80NSSC18K0177. We are also grateful to two anonymous reviewers for their insightful comments and suggestions that greatly improved this paper.

Edited by: Julia Uitz

Reviewed by: two anonymous referees

References

- Álvarez-Romero, J. G., Devlin, M., da Silva, E. T., Petus, C., Ban, N. C., Pressey, R. L., Kool, J., Roberts, J. J., Cerdeira-Estrada, S., and Wenger, A. S.: A novel approach to model exposure of coastal-marine ecosystems to riverine flood plumes based on remote sensing techniques, *J. Environ. Manage.*, 119, 194–207, 2013.
- Aurin, D. A. and Dierssen, H. M.: Advantages and limitations of ocean color remote sensing in CDOM-dominated, mineral-rich coastal and estuarine waters, *Remote Sens. Environ.*, 125, 181–197, 2012.
- Bailey, S. W., Franz, B. A., and Werdell, P. J.: Estimation of near-infrared water-leaving reflectance for satellite ocean color data processing, *Optics Express*, 18, 7521–7527, <https://doi.org/10.1364/OE.18.007521>, 2010.
- Brewin, R. J. W., Sathyendranath, S., Müller, D., Brockmann, C., Deschamps, P.-Y., Devred, E., Doerffer, R., Fomferra, N., Franz, B., Grant, M., Groom, S., Horseman, A., Hu, C., Krasemann, H., Lee, Z., Maritorena, S., Mélin, F., Peters, M., Platt, T., Regner, P., Smyth, T., Steinmetz, F., Swinton, J., Werdell, J., and White III, G. N.: The Ocean Colour Climate Change Initiative: III. A round-robin comparison on in-water bio-optical algorithms, *Remote Sens. Environ.*, 162, 271–294, 2015.
- Bricker, S. B., Longstaff, B., Dennison, W., Jones, A., Boicourt, K., Wicks, C., and Woerner, J.: Effects of nutrient enrichment in the nation's estuaries: a decade of change, *Harmful Algae*, 8, 21–32, 2008.
- Carvalho, G. A., Minnett, P. J., Banzon, V. F., Baringer, W., and Heil, C. A.: Long-term evaluation of three satellite ocean color algorithms for identifying harmful algal blooms (*Karenia brevis*) along the west coast of Florida: A matchup assessment, *Remote Sens. Environ.*, 115, 1–18, 2011.
- Castillo, K. D. and Lima, F. P.: Comparison of in situ and satellite-derived (MODIS-Aqua/Terra) methods for assessing temperatures on coral reefs, *Limnol. Oceanogr.-Meth.*, 8, 107–117, 2010.
- Cavanaugh, K. C., Siegel, D. A., Reed, D. C., and Dennison, P. E.: Environmental controls of giant-kelp biomass in the Santa Barbara Channel, California, *Mar. Ecol.-Prog. Ser.*, 429, 1–17, 2011.
- Chen, J., Quan, W., Wen, Z., and Cui, T.: An improved three-band semi-analytical algorithm for estimating chlorophyll-*a* concentration in highly turbid coastal waters: a case study of the Yellow River estuary, China, *Environ. Earth Sci.*, 69, 2709–2719, 2013.
- Chen, S., Huang, W., Wang, H., and Li, D.: Remote sensing assessment of sediment re-suspension during Hurricane Frances in Apalachicola Bay, USA, *Remote Sens. Environ.*, 113, 2670–2681, 2009.
- Chen, S. and Zhang, T.: Evaluation of a QAA-based algorithm using MODIS land bands data for retrieval of IOPs in the Eastern China Seas, *Opt. Express*, 23, 13953–13971, <https://doi.org/10.1364/OE.23.013953>, 2015.
- D'Sa, E. J. and Miller, R. L.: Bio-optical properties in waters influenced by the Mississippi River during low flow conditions, *Remote Sens. Environ.*, 84, 538–549, 2003.
- D'Sa, E. J., Miller R. L., and Del Castillo, C.: Bio-optical properties and ocean color algorithms for coastal waters influenced by the Mississippi River during a cold front, *Appl. Optics*, 45, 7410–7428, 2006.
- D'Sa, E. J., Miller, R. L., and McKee, B. A.: Suspended particulate matter dynamics in coastal waters from ocean color: Application to the northern Gulf of Mexico, *Geophys. Res. Lett.*, 34, L23611, <https://doi.org/10.1029/2007GL031192>, 2007.
- D'Sa, E. J., Overton, E. B., Lohrenz, S. E., Maiti, K., Turner, R. E., and Freeman, A.: Changing dynamics of dissolved organic matter fluorescence in the northern Gulf of Mexico following the Deepwater Horizon oil spill, *Environ. Sci. Technol.*, 50, 4940–4950, 2016.
- D'Sa, E. J., Joshi, I. D., and Liu, B.: Galveston Bay and coastal ocean optical-geochemical response to Hurricane Harvey from VIIRS ocean color, submitted, 2018.
- Dong, Q., Shang, S., and Lee, Z.: An algorithm to retrieve absorption coefficient of chromophoric dissolved organic matter from ocean color, *Remote Sens. Environ.*, 128, 259–267, 2013.
- Doxaran, D., Froidefond, J. M., Lavender, S., and Castaing, P.: Spectral signature of highly turbid waters: Application with SPOT data to quantify suspended particulate matter concentrations, *Remote Sens. Environ.*, 81, 149–161, 2002.
- Gordon, H. R., Brown, O. B., Evans, R. H., Brown, J. W., Smith, R. C., Baker, K. S., and Clark, D. K.: A semianalytic radiance model of ocean color, *J. Geophys. Res.-Atmos.*, 93, 10909–10924, 1988.
- Guthrie, C. G., Matsumoto, J., and Solis, R. S.: Analysis of the influence of water plan strategies on inflows and salinity in Galveston Bay, United States Army Corps of Engineers, Texas Water Development Board, Austin, Texas, 71 pp., 2012.
- Han, B., Loisel, H., Vantrepotte, V., Mériaux, X., Bryère, P., Ouilon, S., Dessailly, D., Xing, Q., and Zhu, J.: Development of a semi-analytical algorithm for the retrieval of suspended particulate matter from remote sensing over clear to very turbid waters, *Remote Sens.*, 8, 211, <https://doi.org/10.3390/rs8030211>, 2016.
- Haynes, D., Brodie, J., Waterhouse, J., Bainbridge, Z., Bass, D., and Hart, B.: Assessment of the water quality and ecosystem health of the Great Barrier Reef (Australia): Conceptual models, *Environ. Manage.*, 40, 993–1003, <https://doi.org/10.1007/s00267-007-9009-y>, 2007.
- Hu, C., Luerssen, R., Muller-Karger, F. E., Carder, K. L., and Heil, C. A.: On the remote monitoring of *Karenia brevis* blooms of the west Florida shelf, *Cont. Shelf Res.*, 28, 159–176, 2008.
- Hu, C., Murch, B., Corcoran, A. A., Zheng, L., Barnes, B. B., Weisberg, R. H., Atwood, K., and Lenos, J. M.: Developing a smart semantic web with linked data and models for near-real-time mon-

- itoring of red tides in the Eastern Gulf of Mexico, *IEEE Syst. J.*, 10, 1282–1290, 2016.
- IOCCG: Remote Sensing of Inherent Optical Properties: Fundamentals, Tests of Algorithms, and Applications, Reports of the International Ocean-Colour Coordinating Group, No. 5, IOCCG, Dartmouth, Canada, 2006.
- Joshi, I. and D'Sa, E. J.: Seasonal variation of colored dissolved organic matter in Barataria Bay, Louisiana, using combined Landsat and field data, *Remote Sens.*, 7, 12478–12502, 2015.
- Joshi, I. D., D'Sa, E. J., Osburn, C. L., Bianchi, T. S., Ko, D. S., Oviedo-Vargas, D., Arellano, A. R., and Ward, N. D.: Assessing chromophoric dissolved organic matter (CDOM) distribution, stocks, and fluxes in Apalachicola Bay using combined field, VIIRS ocean color, and model observations, *Remote Sens. Environ.*, 191, 359–372, 2017a.
- Joshi, I. D., D'Sa, E. J., Osburn, C. L., and Bianchi, T. S.: Turbidity in Apalachicola Bay, Florida from Landsat 5 TM and Field Data: Seasonal patterns and response to extreme events, *Remote Sens.*, 9, 367, <https://doi.org/10.3390/rs9040367>, 2017b.
- Jutterström, S., Andersson, H. C., Omstedt, A., and Malmaeus, J. M.: Multiple stressors threatening the future of the Baltic Sea-Kattegat marine ecosystem: Implications for policy and management actions, *Mar. Pollut. Bull.*, 86, 468–480, 2014.
- Keith, D., Yoder, J., and Freeman, S.: Spatial and temporal distribution of coloured dissolved organic matter (CDOM) in Narragansett Bay, Rhode Island: implications for phytoplankton in coastal waters, *Estuar. Coast. Shelf S.*, 55, 705–717, 2002.
- Kjelland, M. E., Woodley, C. M., Swannack, T. M., and Smith, D. L.: A review of the potential effects of suspended sediment on fishes: potential dredging-related physiological, behavioral, and transgenerational implications, *Environment Systems and Decisions*, 35, 334–350, <https://doi.org/10.1007/s10669-015-9557-2>, 2015.
- Le, C., Hu, C., English, D., Cannizzaro, J., and Kovach, C.: Climate-driven chlorophyll-*a* changes in a turbid estuary: Observations from satellites and implications for management, *Remote Sens. Environ.*, 130, 11–24, 2013.
- Lee, Z., Carder, K. L., Mobley, C. D., Steward, R. G., and Patch, J. S.: Hyperspectral remote sensing for shallow waters. I. A semi-analytical model, *Appl. Optics*, 37, 6329–6338, 1998.
- Lee, Z., Carder, K. L., Mobley, C. D., Steward, R. G., and Patch, J. S.: Hyperspectral remote sensing for shallow waters: 2. Deriving bottom depths and water properties by optimization, *Appl. Optics*, 38, 3831–3843, 1999.
- Lee, Z., Carder, K. L., and Arnone, R. A.: Deriving inherent optical properties from water color: a multiband quasi-analytical algorithm for optically deep waters, *Appl. Optics*, 41, 5755–5772, 2002.
- Lee, Z., Weidemann, A., Kindle, J., Arnone, R., Carder, K. L., and Davis, C.: Euphotic zone depth: Its derivation and implication to ocean-color remote sensing, *J. Geophys. Res.-Oceans*, 112, C03009, <https://doi.org/10.1029/2006JC003802>, 2007.
- Lee, Z., Lubac, B., Werdell, J., and Arnone, R.: An update of the quasi-analytical algorithm (QAA_v5), International Ocean Color Group Software Report, 1–9, available at: http://www.ioccg.org/groups/Software_OCA/QAA_v5.pdf (last access: 3 July 2018), 2009.
- Lee, Z., Arnone, R., Hu, C., Werdell, P. J., and Lubac, B.: Uncertainties of optical parameters and their propagations in an analytical ocean color inversion algorithm, *Appl. Optics*, 49, 369–381, 2010.
- Lee, Z., Hu, C., Shang, S., Du, K., Lewis, M., Arnone, R., and Brewin, R.: Penetration of UV-visible solar radiation in the global oceans: Insights from ocean color remote sensing, *J. Geophys. Res.-Oceans*, 118, 4241–4255, 2013.
- Lester, L. J. and Gonzalez, L. A.: The State of the Bay: A characterization of the Galveston Bay ecosystem, Texas Commission on Environmental Quality, Galveston Bay Estuary Program, Houston, Texas, 356 pp., 2011.
- Li, J., Yu, Q., Tian, Y. Q., and Becker, B. L.: Remote sensing estimation of colored dissolved organic matter (CDOM) in optically shallow waters, *ISPRS J. Photogramm.*, 128, 98–110, 2017.
- Li, L., Li, L., Song, K., Li, Y., Tedesco, L. P., Shi, K., and Li, Z.: An inversion model for deriving inherent optical properties of inland waters: Establishment, validation and application, *Remote Sens. Environ.*, 135, 150–166, 2013.
- Liu, G., Strong, A. E., Skirving, W., and Arzayus, L. F.: Overview of NOAA coral reef watch program's near-real time satellite global coral bleaching monitoring activities, *Proceedings of the 10th International Coral Reef Symposium*, June 2006, Okinawa, 1783–1793, 2006.
- Loisel, H., Bosc, E., Stramski, D., Oubelkheir, K., and Deschamps, P. Y.: Seasonal variability of the backscattering coefficient in the Mediterranean Sea based on satellite SeaWiFS imagery, *Geophys. Res. Lett.*, 28, 4203–4206, 2001.
- Lohrenz, S., Cai, W.-J., Chen, X., and Tuel, M.: Satellite assessment of bio-optical properties of northern Gulf of Mexico coastal waters following hurricanes Katrina and Rita, *Sensors*, 8, 4135, <https://doi.org/10.3390/s8074135>, 2008.
- Lucena, Z. and Lee, M. T.: Characterization of streamflow, suspended sediment, and nutrients entering Galveston Bay from the Trinity River, Texas, May 2014–December 2015: U.S. Geological Survey Scientific Investigations Report 2016–5177, 38 pp., 2017.
- Matsumoto, K., Honda, M. C., Sasaoka, K., Wakita, M., Kawakami, H., and Watanabe, S.: Seasonal variability of primary production and phytoplankton biomass in the western Pacific subarctic gyre: control by light availability within the mixed layer, *J. Geophys. Res.-Oceans*, 119, 6523–6534, 2014.
- Miller, R. L. and McKee, B. A.: Using MODIS Terra 250 m imagery to map concentrations of total suspended matter in coastal waters, *Remote Sens. Environ.*, 93, 259–266, 2004.
- Minu, P., Lotliker, A. A., Shaju, S. S., Santhosh Kumar, B., Ashraf, P. M., and Meenakumari, B.: Effect of optically active substances and atmospheric correction schemes on remote-sensing reflectance at a coastal site off Kochi, *Int. J. Remote Sens.*, 35, 5434–5447, <https://doi.org/10.1080/01431161.2014.926420>, 2014.
- Mishra, S., Mishra, D. R., Lee, Z., and Tucker, C. S.: Quantifying cyanobacterial phycocyanin concentration in turbid productive waters: A quasi-analytical approach, *Remote Sens. Environ.*, 133, 141–151, 2013.
- Mitchell, C., Cunningham, A., and McKee, D.: Remote sensing of particulate absorption coefficients and their biogeochemical interpretation: A case study in the Irish Sea, *Remote Sens. Environ.*, 152, 74–82, 2014.

- Mobley, C. D.: Estimation of the remote-sensing reflectance from above-surface measurements, *Appl. Optics*, 38, 7442–7455, <https://doi.org/10.1364/AO.38.007442>, 1999.
- Mobley, C. D. and Sundman, L. K.: *Hydrolight – Ecolight 5.2 user's guide*, Sequoia Scientific, Inc., Bellevue, WA, 2013.
- Morel, A. and Gentili, B.: Diffuse reflectance of oceanic waters: its dependence on Sun angle as influenced by the molecular scattering contribution, *Appl. Optics*, 30, 4427–4438, 1991.
- Morel, A. and Gentili, B.: Diffuse reflectance of oceanic waters. II. Bidirectional aspects, *Appl. Optics*, 32, 6864–6879, 1993.
- Morel, A. and Gentili, B.: Diffuse reflectance of oceanic waters. III. Implication of bidirectionality for the remote-sensing problem, *Appl. Optics*, 35, 4850–4862, <https://doi.org/10.1364/AO.35.004850>, 1996.
- Mueller, J. L., Davis, C., Arnone, R., Frouin, R., Carder, K., Lee, Z., Steward, R., Hooker, S., Mobley, C. D., and McLean, S.: Above-water radiance and remote sensing reflectance measurements and analysis protocols. *Ocean Optics Protocols for Satellite Ocean Color Sensor Validation, Revision 4, Volume III: Radiometric Measurements and Data Analysis Protocols*, NASA, Goddard Space Flight Space Center, Greenbelt, Maryland, 21–31, 2003.
- Naik, P., D'Sa, E. J., Grippo, M., Condrey, R., and Fleeger, J.: Absorption properties of shoal-dominated waters in the Atchafalaya Shelf, Louisiana, USA, *Int. J. Remote Sens.*, 32, 4383–4406, 2011.
- Nechad, B., Ruddick, K. G., and Park, Y.: Calibration and validation of a generic multisensor algorithm for mapping of total suspended matter in turbid waters, *Remote Sens. Environ.*, 114, 854–866, 2010.
- Neukermans, G., Ruddick, K., Loisel, H., and Roose, P.: Optimization and quality control of suspended particulate matter concentration measurement using turbidity measurements, *Limnol. Oceanogr.-Meth.*, 10, 1011–1023, 2012.
- Novoa, S., Doxaran, D., Ody, A., Vanhellemont, Q., Lafon, V., Lubac, B., and Gernez, P.: Atmospheric corrections and multi-conditional algorithm for multi-sensor remote sensing of suspended particulate matter in low-to-high turbidity levels coastal waters, *Remote Sens.*, 9, 61, <https://doi.org/10.3390/rs9010061>, 2017.
- Pan, X., Mannino, A., Russ, M. E., Hooker, S. B., and Harding Jr., L. W.: Remote sensing of phytoplankton pigment distribution in the United States northeast coast, *Remote Sens. Environ.*, 114, 2403–2416, 2010.
- Pedersen, T. M., Gallegos, C. L., and Nielsen, S. L.: Influence of near-bottom re-suspended sediment on benthic light availability, *Estuar. Coast. Shelf S.*, 106, 93–101, 2012.
- Pitarch, J., Bellacicco, M., Volpe, G., Colella, S., and Santoleri, R.: Use of the quasi-analytical algorithm to retrieve backscattering from in-situ data in the Mediterranean Sea, *Remote Sens. Lett.*, 7, 591–600, <https://doi.org/10.1080/2150704X.2016.1171922>, 2016.
- Pu, R. and Bell, S.: Mapping seagrass coverage and spatial patterns with high spatial resolution IKONOS imagery, *Int. J. Appl. Earth Obs.*, 54, 145–158, 2017.
- Qi, L., Hu, C., Cannizzaro, J., Corcoran, A. A., English, D., and Le, C.: VIIRS observations of a *Karenia brevis* bloom in the north-eastern Gulf of Mexico in the absence of a fluorescence band, *IEEE Geosci. Remote S.*, 12, 2213–2217, 2015.
- Qing, S., Tang, J., Cui, T., and Zhang, J.: Retrieval of inherent optical properties of the Yellow Sea and East China Sea using a quasi-analytical algorithm, *Chin. J. Oceanol. Limn.*, 29, 33–45, 2011.
- Ralph, P., Durako, M. J., Enriquez, S., Collier, C., and Doblin, M.: Impact of light limitation on seagrasses, *J. Exp. Mar. Biol. Ecol.*, 350, 176–193, 2007.
- Ramsey III, E., Rangoonwala, A., Suzuoki, Y., and Jones, C. E.: Oil detection in a coastal marsh with polarimetric synthetic aperture radar (SAR), *Remote Sens.*, 3, 2630–2662, 2011.
- Ruddick, K. G., De Cauwer, V., Park, Y.-J., and Moore, G.: Seaborne measurements of near infrared water-leaving reflectance: The similarity spectrum for turbid waters, *Limnol. Oceanogr.*, 51, 1167–1179, 2006.
- Singh, S., D'Sa, E. J., and Swenson, E. M.: Chromophoric dissolved organic matter (CDOM) variability in Barataria Basin using excitation–emission matrix (EEM) fluorescence and parallel factor analysis (PARAFAC), *Sci. Total Environ.*, 408, 3211–3222, 2010.
- Stramski, D., Reynolds, R. A., Kahru, M., and Mitchell, B. G.: Estimation of particulate organic carbon in the ocean from satellite remote sensing, *Science*, 285, 239–242, 1999.
- Uitz, J., Claustre, H., Gentili, B., and Stramski, D.: Phytoplankton class-specific primary production in the world's oceans: seasonal and interannual variability from satellite observations, *Global Biogeochem. Cy.*, 24, GB3016, <https://doi.org/10.1029/2009GB003680>, 2010.
- Wang, H., Huang, W., Harwell, M. A., Edmiston, L., Johnson, E., Hsieh, P., Milla, K., Christensen, J., Stewart, J., and Liu, X.: Modeling oyster growth rate by coupling oyster population and hydrodynamic models for Apalachicola Bay, Florida, USA, *Ecol. Model.*, 211, 77–89, 2008.
- Werdell, P. J., Bailey, S., Fargion, G., Pietras, C., Knobelspiesse, K., Feldman, G., and McClain, C.: Unique data repository facilitates ocean color satellite validation, *EOS T. Am. Geophys. Un.*, 84, 377–387, 2003.
- Werdell, P. J. and Bailey, S. W.: An improved in-situ bio-optical data set for ocean color algorithm development and satellite data product validation, *Remote Sens. Environ.*, 98, 122–140, 2005.
- Werdell, P. J., Franz, B. A., and Bailey, S. W.: Evaluation of short-wave infrared atmospheric correction for ocean color remote sensing of Chesapeake Bay, *Remote Sens. Environ.*, 114, 2238–2247, 2010.
- Zhang, X. and Gray, D. J.: Backscattering by very small particles in coastal waters, *J. Geophys. Res.-Oceans*, 120, 6914–6926, <https://doi.org/10.1002/2015JC010936>, 2015.
- Zhang, X., Twardowski, M., and Lewis, M.: Retrieving composition and sizes of oceanic particle subpopulations from the volume scattering function, *Appl. Optics*, 50, 1240–1259, <https://doi.org/10.1364/AO.50.001240>, 2011.
- Zhao, J., Temimi, M., Ghedira, H., and Hu, C.: Exploring the potential of optical remote sensing for oil spill detection in shallow coastal waters – a case study in the Arabian Gulf, *Opt. Express*, 22, 13755–13772, <https://doi.org/10.1364/OE.22.013755>, 2014.
- Zheng, G., Stramski, D., and Reynolds, R. A.: Evaluation of the Quasi-Analytical Algorithm for estimating the inherent optical properties of seawater from ocean color: Comparison of Arctic and lower-latitude waters, *Remote Sens. Environ.*, 155, 194–209, 2014.

Zhu, W., Yu, Q., Tian, Y. Q., Chen, R. F., and Gardner, G. B.: Estimation of chromophoric dissolved organic matter in the Mississippi and Atchafalaya River plume regions using above-surface hyperspectral remote sensing, *J. Geophys. Res.-Oceans*, 116, C02011, <https://doi.org/10.1029/2010JC006523>, 2011.

Zielinski, O., Busch, J. A., Cembella, A. D., Daly, K. L., Engelbrektsson, J., Hannides, A. K., and Schmidt, H.: Detecting marine hazardous substances and organisms: sensors for pollutants, toxins, and pathogens, *Ocean Sci.*, 5, 329–349, <https://doi.org/10.5194/os-5-329-2009>, 2009.